

Connectivity Structure and Dynamics of Nonlinear Recurrent Neural Networks

David G. Clark,^{1,*} Owen Marschall,¹ Alexander van Meegen,² and Ashok Litwin-Kumar^{1,†}

¹*Zuckerman Institute, Columbia University, New York, NY 10027, USA*

²*Center for Brain Science, Harvard University, Cambridge, MA 02138, USA*

(Dated: September 4, 2024)

We develop a theory to analyze how structure in connectivity shapes the high-dimensional, internally generated activity of nonlinear recurrent neural networks. Using two complementary methods – a path-integral calculation of fluctuations around the saddle point, and a recently introduced two-site cavity approach – we derive analytic expressions that characterize important features of collective activity, including its dimensionality and temporal correlations. To model structure in the coupling matrices of real neural circuits, such as synaptic connectomes obtained through electron microscopy, we introduce the random-mode model, which parameterizes a coupling matrix using random input and output modes and a specified spectrum. This model enables systematic study of the effects of low-dimensional structure in connectivity on neural activity. These effects manifest in features of collective activity, that we calculate, and can be undetectable when analyzing only single-neuron activities. We derive a relation between the effective rank of the coupling matrix and the dimension of activity. By extending the random-mode model, we compare the effects of single-neuron heterogeneity and low-dimensional connectivity. We also investigate the impact of structured overlaps between input and output modes, a feature of biological coupling matrices. Our theory provides tools to relate neural-network architecture and collective dynamics in artificial and biological systems.

I. INTRODUCTION

Nonlinear recurrent neural networks are used in neuroscience as models of neural-circuit dynamics [1–3] and in machine learning as systems for sequence processing [4–7]. Such networks can generate complex, time-varying activity in the absence of external input [8, 9]. This high-dimensional chaotic activity, first analyzed by Sompolinsky *et al.* [10], has served as a model for asynchronous cortical dynamics observed *in vivo*. Moreover, initializing recurrent neural networks so that they exhibit chaotic dynamics has been shown to facilitate subsequent learning [11–13].

Theoretical studies often focus on large recurrent neural networks with independent and identically distributed (i.i.d.) couplings. However, the structure of real-world networks, including neural circuits, typically deviates substantially from this assumption [14]. Many real-world networks show approximate low-rank structure, meaning that their connectivity is well described by a number of rank-one components that is smaller than the number of units in the network [15]. Often, networks have “smooth low-rank” or “effectively low-rank” structure in which the strengths of these rank-one components do not exhibit a hard cutoff and instead decay smoothly, with a more rapid falloff than in networks with i.i.d. couplings. This can arise when connections between units depend on their distance in physical space, or in a low-dimensional feature space [16–18]. Such low-rank structure can also emerge when artificial neural networks are trained on tasks [19, 20].

To illustrate this, we examined a central-brain connectome of the fruit fly *Drosophila melanogaster* [21] (Fig. 1a).

We estimated strengths from synaptic counts, assigned coupling signs based on predicted neurotransmitter types [22], and normalized the couplings (Fig. 1b; Appendix B). We analyzed the network’s structure using its singular value decomposition (SVD), which expresses the connectivity as a sum of rank-one components, with the strength of each component given by the corresponding singular value. The singular values decay much more quickly than those of an i.i.d. matrix of the same size, which follow a universal form that does not depend on details of the single-element distribution (Fig. 1c). We quantify this decay rate using the participation ratio of the squared singular-value spectrum (Sec. IID 1). For this connectome, the participation ratio is 0.18, much lower than the value of 0.5 for an i.i.d. matrix, demonstrating that this network has a much lower-rank structure than would be expected for i.i.d. couplings.

In neuroscience, the importance of connectivity lies in its role in controlling neural activity. To this end, dynamical mean-field theory (DMFT) has been used to analyze activity in large recurrent neural networks, focusing on single-neuron properties such as the autocovariance function. However, recent neuroscience studies have highlighted the significance of geometric or other collective properties that emerge only when examining the simultaneous activity of large neuronal populations [23, 24]. Given neural data, these properties are often analyzed using dimensionality reduction techniques like principal component analysis. Recent advances have extended DMFT techniques to analytically characterize these collective features in nonlinear network models producing high-dimensional chaotic activity [25]. Other studies have addressed simpler cases, including linear networks driven by noise [26–29] and nonlinear networks producing low-dimensional activity [30, 31]. A key quantity of interest is the *dimension* of activity, which quantifies the number

* dgc2138@cumc.columbia.edu

† a.litwin-kumar@columbia.edu

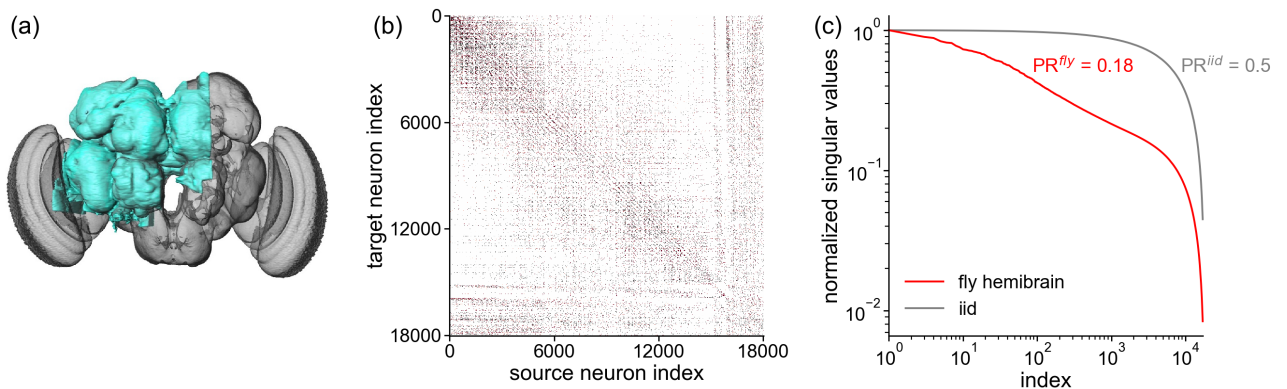


FIG. 1. Analysis of *Drosophila* central brain connectome. (a) Volume of fly brain for which reconstruction was performed (blue; reproduced from [21]). (b) Visualization of the full normalized coupling matrix. (c) Singular value spectra of the normalized coupling matrix (red) and an i.i.d. random matrix (gray). The fly connectome exhibits a smooth spectrum that decays quickly, corresponding to a reduced participation ratio. $N = 18028$ neurons.

of high-variance activity modes. This metric reflects a network’s capacity for complex computations and representations, and influences its learning and generalization capabilities [32, 33]. Despite these advances, the analytical calculation of activity dimension in nonlinear networks has been limited to i.i.d. connectivity, or connectivity with simple correlations between reciprocal synapses, and thus cannot be performed for networks with more realistic structures (Fig. 1c). To address this gap, we study networks with smooth low-rank parameterizations of couplings, and develop DMFT tools to analyze collective activity in such networks. We show that, in certain cases, the effects of structure in connectivity are not evident in single-neuron activity, but instead revealed through dramatic changes in properties of collective activity that we show how to compute.

This paper has two main contributions. The first is a new path-integral calculation of a specific four-point function of network activity, originally defined by Clark *et al.* [25]. This function captures statistics describing collective activity, including its dimensionality. In Secs. II A–II C, we describe the recurrent-network model and define this four-point function. We explain its connection to collective activity features, including the activity dimension and timescales of principal components, and review its calculation in i.i.d. networks. In Secs. III A–III D, we introduce the new path-integral calculation and apply it to both the i.i.d. model and a model with correlations between reciprocal pairs of synapses.

The second contribution is a tractable model of neural-network coupling matrices that we call the random-mode model. In Sec. II D, we define this model, in which couplings are generated as a sum of rank-one outer products of random input and output modes with component-specific strengths. In Sec. II D 1, we demonstrate that parameterizing these strengths provides control over the singular value spectrum of the coupling matrix, enabling investigation of the interplay between global connectivity structure and network dynamics. In Sec. III E, we calculate the

two- and four-point functions for the random-mode model using the path-integral approach. This analysis reveals a bipartite coupling between neurons and latent variables. In Sec. III F, we interpret the resulting formulas for the four-point function, which show how the effective rank of the coupling matrix controls the dimension of activity. In Sec. IV, we analyze limiting cases of the random-mode model, illustrating that a vanishing effective rank leads to vanishing activity dimension. In Sec. V, we show that the same results can be obtained using an intuitive two-site cavity method. In Sec. VI, we study the behavior of a generalization of the random-mode model featuring heterogeneity among single-neuron properties and contrast the effects with those of low-rank structure in the connectivity. Finally, in Sec. VII, we incorporate a simple form of overlaps between input and output modes into the model, which we anticipate to be crucial for describing neural computations.

II. MODEL AND SUMMARY STATISTICS

A. Recurrent neural network model

We study a recurrent neural network of N neurons. Each neuron is characterized by its pre-activation $x_i(t)$ and activation $\phi_i(t)$, where $i = 1, \dots, N$. The activations are related to the pre-activations through a nonlinear function $\phi(x)$, with $\phi_i(t) = \phi(x_i(t))$. While our results are agnostic to the form of the nonlinearity, when comparing theory and simulations we use $\phi(x) = \text{erf}(\sqrt{\pi}x/2)$, which is similar to the more conventional $\phi(x) = \tanh(x)$ but allows for analytical evaluation of Gaussian integrals. The network dynamics are governed by

$$T[x_i](t) = \sum_j J_{ij} \phi_j(t), \quad (1)$$

where J_{ij} is the coupling from neuron j to neuron i , and $T[\cdot]$ is a causal functional describing single-neuron dynamics. A canonical choice is

$$T[x](t) = (1 + \partial_t)x(t), \quad (2)$$

resulting in low-pass filtering of the input. We measure time in units of the time constant that would appear in front of ∂_t .

B. Correlation functions

1. Two-point functions

To characterize the network dynamics, we introduce several types of two-point correlation functions. Let $a \in \{x, \phi\}$ denote either the pre-activations or activations. We first define the neuron- and time-averaged covariance:

$$C^a(\tau) = \frac{1}{N} \sum_i \langle a_i(t)a_i(t+\tau) \rangle_t. \quad (3)$$

We also define the time-averaged, but not neuron-averaged, covariance; and the neuron-averaged, but not time-averaged, covariance:

$$C_{ij}^a(\tau) = \langle a_i(t)a_j(t+\tau) \rangle_t, \quad (4)$$

$$C^a(t_1, t_2) = \frac{1}{N} \sum_i a_i(t_1)a_i(t_2). \quad (5)$$

For a given τ , the spectra of $C_{ij}^a(\tau)$, with indices i and j , and of $C^a(t_1, t_2 + \tau)$, with indices t_1 and t_2 , are the same (up to a scaling), so spectral properties of one parameter can be computed using the other, a form of duality. For example, the properly scaled trace operations applied to these parameters yield the same result, namely, $C^a(\tau)$.

We also define the response function:

$$S_{ij}^a(t_1, t_2) = \left. \frac{\delta a_i(t_1)}{\delta I_j(t_2)} \right|_{I_j=0}, \quad (6)$$

where $I_j(t)$ is an infinitesimal source term added to the right-hand side of the network dynamics (Eq. 1). In analogy with the covariance functions, we define $S_{ij}^a(\tau)$, $S^a(t_1, t_2)$, and $S^a(\tau)$ to be the response function averaged over time, neurons, or both.

2. Four-point functions

To characterize the dimension and timescales of activity, we define

$$\Psi^a(\boldsymbol{\tau}) = \frac{1}{N} \sum_{i,j} C_{ij}^a(\tau_1)C_{ij}^a(\tau_2), \quad (7)$$

where $\boldsymbol{\tau} = (\tau_1, \tau_2)$. This sum includes the on-diagonal contributions, unlike the quantity computed in Clark *et al.* [25], which we denote by the lower-case $\psi^a(\boldsymbol{\tau})$:

$$\psi^a(\boldsymbol{\tau}) = \frac{1}{N} \sum_{i \neq j} C_{ij}^a(\tau_1)C_{ij}^a(\tau_2). \quad (8)$$

For the type of connectivity we will study, the network exhibits high-dimensional activity such that pairwise covariances are $\mathcal{O}(1/\sqrt{N})$. Thus, in the definition of $\Psi^a(\boldsymbol{\tau})$ (Eq. 7), the on-diagonal contributions (given by $N^{-1} \sum_i C_{ii}^a(\tau_1)C_{ii}^a(\tau_2)$) and off-diagonal contributions (given by $\psi^a(\boldsymbol{\tau})$) are both $\mathcal{O}(1)$.

Leveraging neuron-time duality, $\Psi^a(\boldsymbol{\tau})$ can also be expressed in terms of the time-by-time covariance $C^a(t_1, t_2)$:

$$\Psi^a(\boldsymbol{\tau}) = N \langle C^a(t_1, t_2)C^a(t_1 + \tau_1, t_2 + \tau_2) \rangle_{t_1, t_2}. \quad (9)$$

The neuron-by-neuron (Eq. 7) and time-by-time (Eq. 9) definitions of $\Psi^a(\boldsymbol{\tau})$ form the basis of the cavity and path-integral calculations of this function, respectively.

3. Relating Ψ^a to the dimension and timescales of activity

The dimension of activity can be quantified by the participation ratio of its covariance spectrum [9, 23, 27, 32, 34–38]. To define the participation ratio, we diagonalize the equal-time covariance matrix $C_{ij}^a(0)$ to obtain eigenvectors \mathbf{v}_k^a and eigenvalues λ_k^a , as in principal components analysis. The participation ratio is

$$\text{PR}^a = \frac{1}{N} \frac{(\sum_k \lambda_k^a)^2}{\sum_k (\lambda_k^a)^2}, \quad (10)$$

where we normalized by $1/N$ to obtain an intensive, self-averaging quantity. To see why this provides a useful measure of dimension, consider the case where a fraction w of eigenvalues are equal to a positive constant and the rest are zero. Then, $\text{PR}^a = w$. In practice, the spectrum often has a smooth decay with characteristic decay constant $w \ll 1$ rather than a hard cutoff. In this case the spectrum takes the form $\lambda_k^a = f(k/Nw)$, leading to $\text{PR}^a \approx cw$ where $c = [\int_0^\infty du f(u)]^2 / \int_0^\infty du f^2(u)$ is an order-one constant. Thus, the participation ratio picks out the characteristic decay scale w [36].

An advantageous property of this dimension measure is that it can be expressed in terms of the previously defined two- and four-point correlation functions as

$$\text{PR}^a = \frac{C^a(0)^2}{\Psi^a(0, 0)}. \quad (11)$$

Recall that for the types of connectivity we study, cross-covariances are $\mathcal{O}(1/\sqrt{N})$, so the on- and off-diagonal contributions to $\Psi^a(\boldsymbol{\tau})$ are both order-one (Eq. 7). This leads to PR^a taking a value between 0 and 1 as $N \rightarrow \infty$. Thus, the unnormalized dimension of activity $N \text{PR}^a$ is

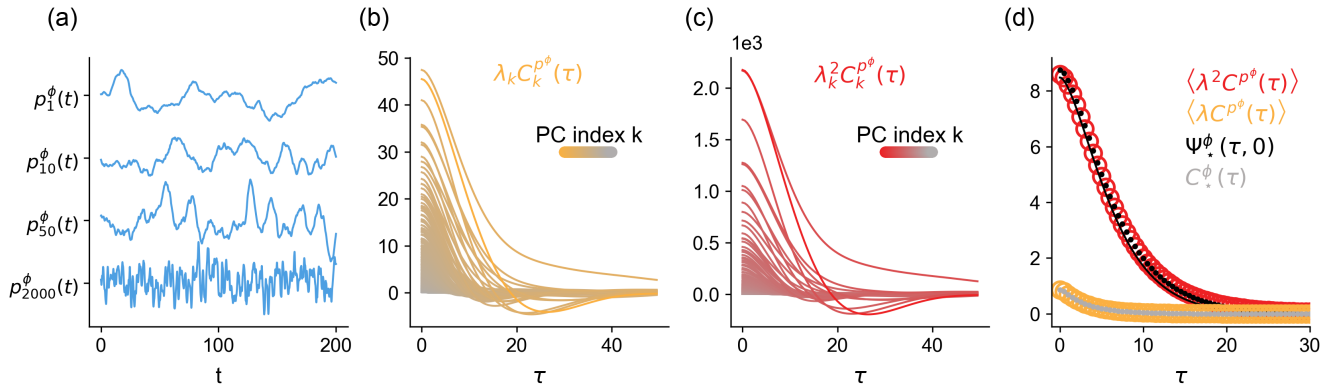


FIG. 2. Relationship between principal component timescales and two- and four-point correlation functions. (a) Example activity traces of principal components $p_k^\phi(t)$. (b) Empirical autocovariance functions for each principal component, weighted by their eigenvalues. (c) Same as (b) but weighted by the squared eigenvalue. (d) Averages over curves in (b) and (c), with comparisons to $C_\star^\phi(\tau)$ and $\Psi_\star^\phi(\tau, 0)$. Dots: simulation results. Lines: theoretical predictions. All panels describe the same network of $N = 4000$ neurons with i.i.d. couplings and $g = 6$.

extensive, i.e., activity is high-dimensional. At the same time, activity does not uniformly occupy all available dimensions, which would require cross-covariances to be smaller than $\mathcal{O}(1/\sqrt{N})$.

Timescales of collective activity can be studied as follows. We define the principal components (PCs) of network activity as

$$p_k^a(t) = \frac{(\mathbf{v}_k^a)^T \mathbf{a}(t)}{\sqrt{\lambda_k^a}}. \quad (12)$$

These PCs are the basis of much of modern analysis of high-dimensional neural data. The PCs all have unit variance but potentially very different characteristic timescales (Fig. 2a). To extract the timescales of just the leading PCs, we compute the PC-averaged covariance, weighted by the squares of the eigenvalues of the corresponding PCs. This gives:

$$\frac{1}{N} \sum_k (\lambda_k^a)^2 \langle p_k^a(t) p_k^a(t + \tau) \rangle_t = \Psi^a(\tau, 0), \quad (13)$$

showing that $\Psi^a(\tau)$ captures the temporal structure of the leading PCs of network activity (Fig. 2c,d). Note that weighting by the eigenvalues themselves, rather than their squares, gives $N^{-1} \sum_k \lambda_k^a \langle p_k^a(t) p_k^a(t + \tau) \rangle_t = C^a(\tau)$, recovering single-neuron information (Fig. 2b,d).

C. Computing the two- and four-point functions in the i.i.d. case

We now review how to compute these two- and four-point functions in a classic network model with i.i.d. couplings \mathbf{J} . The first- and second-order coupling statistics

are:

$$\langle J_{ij} \rangle_{\mathbf{J}} = 0, \quad \langle J_{ij}^2 \rangle_{\mathbf{J}} = \frac{g^2}{N}. \quad (14)$$

The magnitude of a typical coupling is g/\sqrt{N} . We refer to g as the coupling strength. For the canonical dynamics of Eq. 2, the network is quiescent for $g < 1$ and chaotic for $g > 1$, with a sharp phase transition as $N \rightarrow \infty$. In this paper we assume that the network is non-quiescent.

We compute $C^a(t_1, t_2)$ and $\Psi^a(\tau)$ in the limit $N \rightarrow \infty$ under the disorder average. We use the subscript \star to denote such limiting, disorder-averaged values:

$$C_\star^a(t_1, t_2) = \lim_{N \rightarrow \infty} \langle C^a(t_1, t_2) \rangle_{\mathbf{J}}, \quad (15)$$

$$\Psi_\star^a(\tau) = \lim_{N \rightarrow \infty} \langle \Psi^a(\tau) \rangle_{\mathbf{J}}. \quad (16)$$

These values also correspond to the saddle point of a path integral. Both of these functions are self-averaging, meaning that the same values are obtained, up to $\mathcal{O}(1/\sqrt{N})$ fluctuations, when they are computed based on a single realization of a large network. In this paper, we are interested in statistically stationary, temporally fluctuating states such that $C_\star^\phi(t_1, t_2) = C_\star^\phi(t_2 - t_1)$.

The two-point function $C_\star^a(t_1, t_2)$ can be computed through a single-site picture that describes the dynamics of a typical neuron embedded in the rest of the network, with pre-activation $x(t)$ and activation $\phi(t)$. The single-site dynamics are given by

$$T[x](t) = \eta^x(t), \quad (17)$$

where $\eta^x(t)$ is a Gaussian field with mean zero and covariance $g^2 C_\star^\phi(t_1, t_2)$. We denote this by

$$\eta^x \sim \mathcal{GP}(0, g^2 C_\star^\phi). \quad (18)$$

$C_\star^\phi(t_1, t_2)$ is determined self-consistently by enforcing

$$C_\star^\phi(t_1, t_2) = \langle \phi(t_1)\phi(t_2) \rangle_\star, \quad (19)$$

where $\langle \dots \rangle_\star$ denotes an average within this single-site process, i.e., with respect to the Gaussian distribution of $\eta^x(t)$. Once $C_\star^\phi(t_1, t_2)$ has been determined, $C_\star^x(t_1, t_2)$ follows easily. This single-site problem can be derived through either a single-site cavity calculation (see [39]) or a saddle-point condition in a path integral (see [40, 41]). For the i.i.d. couplings considered here, there is a simpler heuristic derivation: in the neuronal input $\sum_j J_{ij}\phi_j(t)$, the correlations between the couplings J_{ij} and dynamic variables $\phi_j(t)$ can be safely neglected to leading order in $1/N$, yielding both Gaussianity of $\eta^x(t)$ by the central limit theorem and the second-order statistics of Eq. 18.

Clark *et al.* [25] first computed $\Psi_\star^a(\boldsymbol{\tau})$ using a dynamic, two-site version of the cavity method, based on the neuron-by-neuron definition (Eq. 7). This method finds $\psi_\star^a(\boldsymbol{\tau})$, the off-diagonal contribution to $\Psi_\star^a(\boldsymbol{\tau})$, noting that the on-diagonal contribution is simply $C_\star^a(\tau_1)C_\star^a(\tau_2)$. A cavity is first created by removing two neurons from the network and allowing the rest of the network, the reservoir, to generate dynamic activity. The cavity neurons are then introduced, and their effect on the reservoir is treated perturbatively. This yields a pair of coupled mean-field equations for the cavity units, generalizing the single-site picture discussed above to a two-site picture. Finally, self-consistency conditions are constructed by recognizing that the cavity pair is statistically equivalent to any reservoir pair. This calculation results in expressions for the four-point function in Fourier space, given by

$$\Psi_\star^\phi(\boldsymbol{\omega}) = \frac{C_\star^\phi(\omega_1)C_\star^\phi(\omega_2)}{|1 - g^2 S_\star^\phi(\omega_1)S_\star^\phi(\omega_2)|^2} \quad (20)$$

for the activations, and

$$\Psi_\star^x(\boldsymbol{\omega}) = C_\star^x(\omega_1)C_\star^x(\omega_2) + |U(\boldsymbol{\omega})|^2 C_\star^\phi(\omega_1)C_\star^\phi(\omega_2) + U(\boldsymbol{\omega})C_\star^{x\phi}(\omega_1)C_\star^{x\phi}(\omega_2) + \text{h.c.}, \quad (21a)$$

$$U(\boldsymbol{\omega}) = \frac{g^2 S_\star^x(\omega_1)S_\star^x(\omega_2)}{1 - g^2 S_\star^\phi(\omega_1)S_\star^\phi(\omega_2)}, \quad (21b)$$

for the pre-activations, where $\boldsymbol{\omega} = (\omega_1, \omega_2)$ and $C_\star^\phi(\omega)$ is a cross-covariance between the pre-activation and activation. Note that if the joint distribution of pre-activations were Gaussian, $\Psi_\star^x(\boldsymbol{\tau})$ and $\Psi_\star^\phi(\boldsymbol{\tau})$ would differ only by a proportionality constant due to Price's theorem [42]. The more complex relationship observed here reflects the non-Gaussian joint statistics across different neurons, which is relevant because the network is nonlinear.

D. Definition of the random-mode model

Many studies have examined the dynamics of networks with i.i.d. couplings, as described in the previous section.

However, the coupling matrices of real-world networks often have approximate low-rank spectral structure, deviating dramatically from the i.i.d. assumption. To analyze networks with such properties, we introduce the random-mode model. This model generates a coupling matrix \mathbf{J} of the form

$$\mathbf{J} = \sum_{a=1}^M D_a \mathbf{L}_a \mathbf{R}_a^T, \quad (22)$$

where \mathbf{R}_a and \mathbf{L}_a are ‘‘input’’ and ‘‘output’’ modes in the neuron space and $D_a > 0$ is a weighting factor called the component strength. The effect of multiplying by \mathbf{J} is to project a neuronal activity vector onto \mathbf{R}_a , scale it by D_a , project the result along \mathbf{L}_a , and sum these contributions for all $a = 1, \dots, M$ (Fig. 3, top). Eq. 22 can be written

$$\mathbf{J} = \mathbf{L} \mathbf{D} \mathbf{R}^T, \quad (23)$$

where \mathbf{L} and \mathbf{R} are $N \times M$ matrices and $\mathbf{D} = \text{diag}(D_1, D_2, \dots, D_M)$.

A crucial modeling choice is how the number of modes, M , scales relative to the network size, N . We consider the limit where both M and N approach infinity while maintaining a fixed ratio,

$$\alpha = \frac{M}{N} = \mathcal{O}(1). \quad (24)$$

This scaling results in *extensive-rank connectivity*, meaning that the rank of \mathbf{J} grows linearly with N . Importantly, choosing α to be small (or choosing the component strengths to decay rapidly; see below) allows for connectivity that is low-rank compared to the number of neurons.

For now, we assume that the matrices \mathbf{L} and \mathbf{R} have independent and identically distributed elements with zero mean and variance $1/N$. We assume these elements are Gaussian, although our results should not depend on the exact form of the single-element density for large N due to the central limit theorem.

A key feature of the random-mode model is that we have full control over the component strengths D_a , which are analogous to the singular values of \mathbf{J} (we make this link precise in Sec. IID 1). We assume only that these component strengths follow a distribution that remains constant as N grows, ensuring a well-defined large- N limit. By varying this distribution, we can explore the impact of the spectral structure of the connectivity on collective features of network activity (Fig. 3, bottom).

We denote the n -th moment of the D_a distribution by

$$r_n = \langle D^n \rangle_D. \quad (25)$$

It will be useful to define the participation ratio,

$$\text{PR}^D = \frac{r_2^2}{r_4}, \quad (26)$$

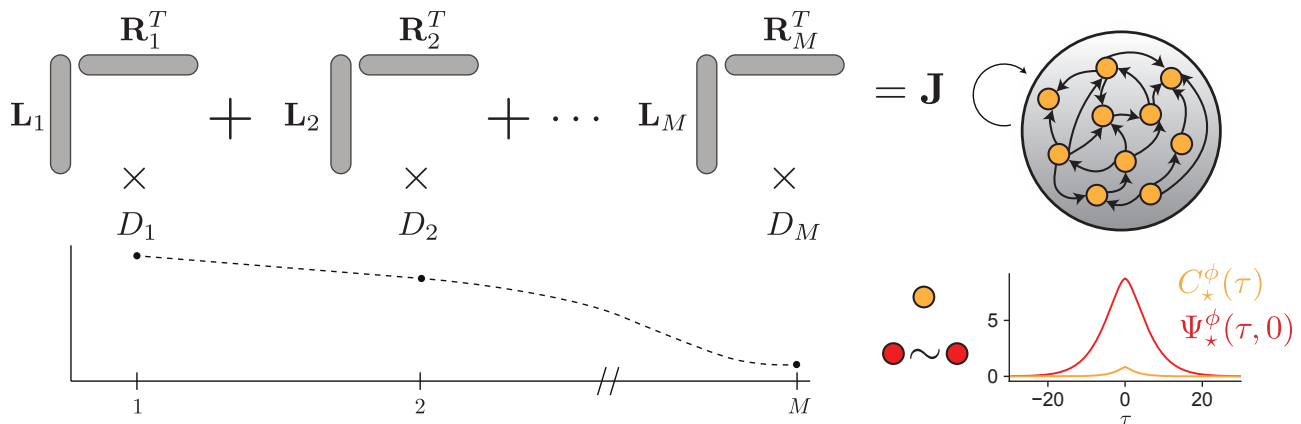


FIG. 3. Schematic of the random-mode model. Upper: Couplings \mathbf{J} are generated as a sum of outer products, $\mathbf{L}_a \mathbf{R}_a^T$, with component strengths D_a . Lower: The two-point function $C_*^\phi(\tau)$ and four-point function $\Psi_*^\phi(\tau, 0)$ are calculated in terms of the statistics of D_a . The two-point function depends only on the effective gain g_{eff} , while the four-point function depends on both g_{eff} and PR^D , the effective dimension of the connectivity determined by the D_a distribution.

from which we define the “effective rank” of the couplings,

$$\text{effective rank} = \alpha \text{PR}^D. \quad (27)$$

This quantity is related to the participation ratio of the singular value spectrum of \mathbf{J} via Eq. 28 below. We will show that this effective rank is a key feature of \mathbf{J} that controls the collective activity structure.

1. Relationship to singular value decomposition

The random-mode model has similarities to the SVD, which decomposes a rank- M matrix \mathbf{J} as $\mathbf{U}\mathbf{S}\mathbf{V}^T$. Here, \mathbf{U} and \mathbf{V} are $N \times M$ matrices whose columns are the left and right singular vectors (or modes), respectively, and $\mathbf{S} = \text{diag}(S_1, S_2, \dots, S_M)$ is a diagonal matrix containing the singular values, $S_a > 0$. The left singular vectors are orthonormal among themselves, as are the right singular vectors (although the left and right singular vectors are generally not orthonormal to each other). In contrast, the columns of \mathbf{L} and \mathbf{R} in the random-mode model have i.i.d. statistics, resulting in random, $\mathcal{O}(1/\sqrt{N})$ overlaps among both within- and across-matrix columns. This i.i.d. assumption offers analytical tractability by eliminating the need to enforce orthonormality, a complicated global constraint (but see [43], who handle random orthonormal matrices in a regression setting). Furthermore, by not explicitly modeling overlaps between \mathbf{L} and \mathbf{R} , the random-mode model parameterizes \mathbf{J} using only the $\mathcal{O}(N)$ component strengths D_a , although such overlaps can be introduced (see Sec. VII).

Given a matrix \mathbf{J} drawn from the random-mode model, we can examine the relationship between the singular values, S_a , and the component strengths, D_a . The non-orthonormality of \mathbf{L} and \mathbf{R} introduces some discrepancy between the two sets of values. We first compare the

participation ratio of the squared singular value spectrum, PR^S , to the effective rank, αPR^D . We find:

$$\text{PR}^S = \frac{\alpha \text{PR}^D}{1 + 2\alpha \text{PR}^D}, \quad (28)$$

where $\text{PR}^S = \langle S^2 \rangle_S^2 / \langle S^4 \rangle_S$, and S are the singular values of \mathbf{J} . This follows from using Wick’s theorem to evaluate the expectations of $\text{tr}(\mathbf{L}\mathbf{D}\mathbf{R}^T\mathbf{R}\mathbf{D}\mathbf{L}^T)$ and $\text{tr}(\mathbf{L}\mathbf{D}\mathbf{R}^T\mathbf{R}\mathbf{D}\mathbf{L}^T\mathbf{L}\mathbf{D}\mathbf{R}^T\mathbf{R}\mathbf{D}\mathbf{L}^T)$ for the numerator and denominator, respectively, of PR^S . For $\alpha \text{PR}^D \ll 1$, $\text{PR}^S = \alpha \text{PR}^D + \mathcal{O}((\alpha \text{PR}^D)^2)$, demonstrating that the component strengths are closely related to the singular values in the low-dimensional regime. In this regime, the random modes approximate an orthonormal set of vectors as $N \rightarrow \infty$ since the $\mathcal{O}(1/\sqrt{N})$ overlaps between modes can be neglected when there are few of them. While we express the analytic results in this paper in terms of αPR^D , Eq. 28 can always be used to translate between αPR^D and PR^S .

We further quantify the discrepancy between singular values and component strengths in the case where $D_a = 1$ for all a . Using methods from free probability theory [44, 45], we compute that the M singular values are distributed over a range with boundaries

$$S_\pm = \sqrt{1 + \frac{5\alpha}{2} - \frac{\alpha^2}{20} \pm \left(1 + \frac{\alpha}{8}\right)^{\frac{3}{2}} \sqrt{8\alpha}}. \quad (29)$$

This is in agreement with large- N simulations (Fig. 4). For small α , $S_\pm = 1 \pm \sqrt{2\alpha} + \mathcal{O}(\alpha)$. While the random-mode model spreads the nonzero singular values over a range, this spreading becomes negligible for small α . More generally, the distributions of D_a and S_a coincide for small αPR^D .

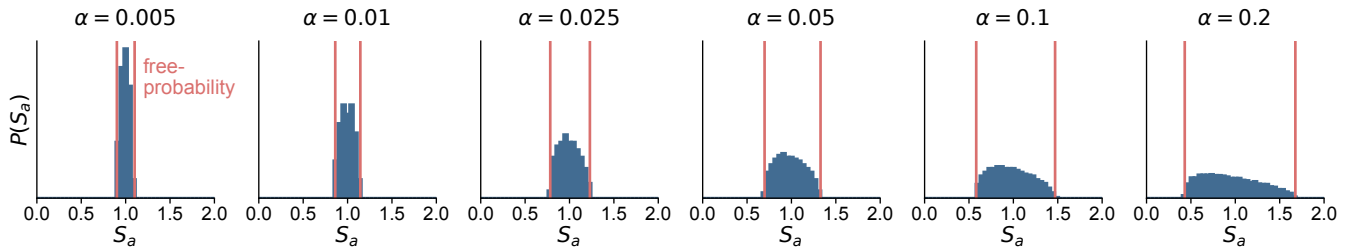


FIG. 4. Distribution of singular values in the random-mode model. Histograms show singular values of \mathbf{LDR}^T with $D_a = 1$ for various α . For $\alpha \ll 1$, the singular values concentrate at one. Vertical lines: prediction of Eq. 29. $N = 5000$.

2. Comparison to low-rank recurrent neural networks

A related parameterization of connectivity has been explored in *low-rank recurrent neural networks*, where the coupling matrix is expressed as a sum of outer products of input modes \mathbf{n}_a and output modes \mathbf{m}_a :

$$\mathbf{J} = \frac{1}{N} \sum_{a=1}^R \mathbf{m}_a \mathbf{n}_a^T, \quad (30)$$

with $R = \mathcal{O}(1)$ being the connectivity rank [30, 31, 46, 47]. In some instances, this low-rank component is added to an i.i.d. matrix modeling unstructured “background” connectivity [30, 46].

Several features separate this approach from the random-mode model. Low-rank recurrent neural networks maintain a constant rank R as $N \rightarrow \infty$, yielding intensive-rank connectivity that models low-dimensional activity, whereas the random-mode model uses extensive-rank connectivity, modeling high-dimensional activity. Furthermore, low-rank recurrent neural networks allow for the most general possible parameterization of overlaps between modes, captured by a $R \times R$ overlap matrix $\mathbf{m}_a^T \mathbf{n}_b$. Specifying such overlaps in the random-mode model would require $\mathcal{O}(N^2)$ parameters, comparable to defining the full coupling matrix. To reduce parameter complexity, the random-mode model specifies only the variances of mode components via the component strengths D_a , disregarding overlaps. This substantially reduces parameter count while preserving interesting network dynamics. In Sec. VII, we introduce $\mathcal{O}(N)$ additional parameters describing a restricted overlap structure among modes, specifying only diagonal elements of the overlap matrix. Further possible overlap forms are discussed in Sec. VIII.

The mean-field descriptions of network dynamics produced by these connectivities also differ markedly. In low-rank recurrent neural networks, low-dimensional network activity is described by a finite set of order parameters representing projections of network activity onto input modes \mathbf{n}_a , obeying effective nonlinear dynamics. Conversely, the extensive-rank connectivity in the random-mode model generates high-dimensional chaotic activity, described by covariance functions capturing temporal fluctuations. While the random-mode model’s mean-field analysis introduces latent variables given by projections

of network activity onto input modes, their extensive number precludes their use as order parameters.

A final distinction lies in the scaling of the coupling matrix \mathbf{J} and its implications for the alignment of activity with connectivity. In low-rank recurrent neural networks, elements of \mathbf{J} scale as $\mathcal{O}(1/N)$ and the input-output mode overlaps are $\mathcal{O}(1)$, resulting in strong $\mathcal{O}(1)$ alignment of network activity with input modes. This is reminiscent of the rich regime of neural networks [48–51]. Conversely, in the random-mode model, the elements of \mathbf{J} scale as $\mathcal{O}(1/\sqrt{N})$ and the input-output mode overlaps are $\mathcal{O}(1/\sqrt{N})$, leading to weak $\mathcal{O}(1/\sqrt{N})$ alignment of network activity with any given input mode; the pre-activations are $\mathcal{O}(1)$ since each neuron combines input from $\mathcal{O}(N)$ modes. This is reminiscent of the lazy regime of neural networks [49, 52, 53].

III. PATH-INTEGRAL CALCULATION OF THE TWO- AND FOUR-POINT FUNCTIONS

The path-integral approach provides a systematic framework for analyzing neural-network dynamics, allowing for controlled approximations such as $1/N$ expansions [41, 54–56]. In this section, we demonstrate how to formulate the calculation of the four-point function $\Psi_*^a(\boldsymbol{\tau})$ within this formalism, allowing us to solve complex models more efficiently than the two-site cavity method by following a straightforward procedure whose steps we outline at the end of Sec. III C.

A. Relating Ψ^a to fluctuations of the time-by-time covariance

To cast the problem in the language of path integrals, we turn to the time-by-time definition of $\Psi^a(\boldsymbol{\tau})$, given by Eq. 9. If the time-by-time covariance $C^a(t_1, t_2)$ were equal to its limiting value, $C_*^a(t_2 - t_1)$, we would have $\Psi_*^a(\boldsymbol{\tau}) \stackrel{?}{=} N \langle C_*^a(t_2 - t_1) C_*^a(t_2 - t_1 + \tau_2 - \tau_1) \rangle_{t_1, t_2} = 0$ since, for large time differences, $C_*^a(t_2 - t_1)$, decays exponentially in $|t_2 - t_1|$ [10]. However, based on the neuron-by-neuron definition, Eq. 7, $\Psi_*^a(\boldsymbol{\tau})$ is clearly a nonzero, order-one quantity. This apparent contradiction is resolved by considering fluctuations around the saddle point.

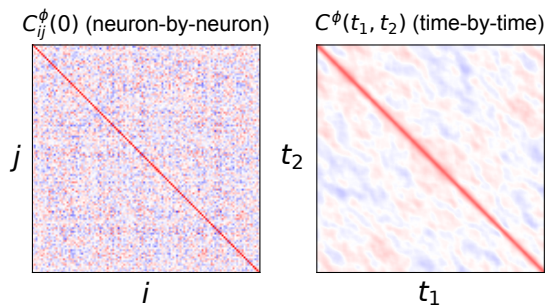


FIG. 5. Neuron-time duality and its relation to the dimension of activity. Both plots are based on the same simulation of a network of $N = 2500$ neurons with $g = 2.25$ and i.i.d. couplings. The dimension can be computed either by computing the statistics of the off-diagonals of the neuron-by-neuron covariance $C_{ij}^\phi(0)$ (left), or by computing the fluctuations away from the translation-invariant mean-field form of the time-by-time covariance $C^\phi(t_1, t_2)$ (right).

The necessity of these fluctuations becomes clear when viewed through the lens of neuron-time duality. The presence of nonzero pairwise covariances $C_{ij}^a(0)$ indicates low-dimensional structure in the system. Equivalently, this structure manifests as the system revisiting similar states in phase space over time, resulting in nonzero temporal covariance $C^a(t_1, t_2)$ even for large time differences $|t_2 - t_1| \gg 1$ (Fig. 5). To capture this behavior, we define fluctuations around the saddle point as

$$\delta C^a(t_1, t_2) = C^a(t_1, t_2) - C_\star^a(t_2 - t_1). \quad (31)$$

We express $\Psi^a(\boldsymbol{\tau})$ purely in terms of these fluctuations as

$$\Psi^a(\boldsymbol{\tau}) = N \langle \delta C^a(t_1, t_2) \delta C^a(t_1 + \tau_1, t_2 + \tau_2) \rangle_{t_1, t_2}, \quad (32)$$

noting that terms involving $C_\star^a(t_2 - t_1)$ vanish at large time differences. Our task, therefore, is to compute the covariance of the fluctuations, $\delta C^a(t_1, t_2)$, captured by

$$\begin{aligned} N \langle \delta C^a(t_1, t_2) \delta C^a(t_3, t_4) \rangle_\star \\ = \lim_{N \rightarrow \infty} N \langle \delta C^a(t_1, t_2) \delta C^a(t_3, t_4) \rangle_{\mathbf{J}}. \end{aligned} \quad (33)$$

Then, to compute $\Psi_\star^a(\boldsymbol{\tau})$, we use the temporal limits

$$\begin{aligned} t_3 = t_1 + \tau_1, & & |t_2 - t_1| \rightarrow \infty, \\ t_4 = t_2 + \tau_2, & & \tau_1, \tau_2 \sim \mathcal{O}(1). \end{aligned} \quad (34)$$

B. Path-integral formalism and two-point functions

Given any fixed \mathbf{J} , we express the network dynamics using a path integral in the Martin-Siggia-Rose/Janssen-De

Dominicis-Peliti formalism [57]:

$$Z[\mathbf{J}] = \int \mathcal{D}\mathbf{x} \int \mathcal{D}\hat{\mathbf{x}} \exp \left(i \sum_i \hat{x}_i T[x_i] - i \sum_{i,j} J_{ij} \hat{x}_j \phi_j \right), \quad (35)$$

where suppressed time indices imply time integrals, e.g., $\hat{x}_i \phi_j = \int dt \hat{x}_i(t) \phi_j(t)$. Here, $\hat{x}_i(t)$ is a field conjugate to $x_i(t)$ that enforces the network's equations of motion (Eq. 1). This path integral serves as a generating function for moments of dynamic variables: by adding source terms $i(b_i x_i + \hat{b}_i \hat{x}_i)$ to the action, derivatives of $Z[\mathbf{J}]$ with respect to b_i and \hat{b}_i produce correlation and response functions, respectively (these sources are not needed for our purposes). In this paper, we keep track of the path integral up to non-physically meaningful multiplicative factors. For a review of this path-integral formalism applied to neural networks, see [40, 41, 58]. To obtain the typical behavior, we average $Z[\mathbf{J}]$ over \mathbf{J} , yielding a disorder-averaged path integral Z .

For simplicity, we begin with the i.i.d. model of \mathbf{J} with mean zero and variance g^2/N . After performing the Gaussian integration over \mathbf{J} , we introduce an auxiliary field $C^\phi(t_1, t_2)$, defined by Eq. 5, and its conjugate $\hat{C}^\phi(t_1, t_2)$ to factorize the action across the neuron index i . This leads to a partition function for a statistical field theory involving $C^\phi(t_1, t_2)$ and $\hat{C}^\phi(t_1, t_2)$:

$$Z = \int \mathcal{D}C^\phi \int \mathcal{D}\hat{C}^\phi \exp \left(-N \mathcal{S}[C^\phi, \hat{C}^\phi] \right), \quad (36)$$

where the intensive action is

$$\mathcal{S}[C^\phi, \hat{C}^\phi] = -\frac{1}{2} C^\phi \hat{C}^\phi - \log W[C^\phi, \hat{C}^\phi], \quad (37)$$

and the single-site path integral is

$$\begin{aligned} W[C^\phi, \hat{C}^\phi] &= \int \mathcal{D}x \int \mathcal{D}\hat{x} \\ &\times \exp \left(ixT[\hat{x}] - \frac{g^2}{2} \hat{x} C^\phi \hat{x} - \frac{1}{2} \hat{C}^\phi \hat{x} \phi \right). \end{aligned} \quad (38)$$

In the limit $N \rightarrow \infty$, the saddle point dominates this integral. The derivatives of the action, which are zero at the saddle point, are

$$\frac{\delta \mathcal{S}}{\delta C^\phi(t_1, t_2)} = -\hat{C}^\phi(t_1, t_2) + g^2 \langle \hat{x}(t_1) \hat{x}(t_2) \rangle_W, \quad (39)$$

$$\frac{\delta \mathcal{S}}{\delta \hat{C}^\phi(t_1, t_2)} = -C^\phi(t_1, t_2) + \langle \phi(t_1) \phi(t_2) \rangle_W, \quad (40)$$

where $\langle \dots \rangle_W$ denotes an average within the dynamic process described by $W[C^\phi, \hat{C}^\phi]$. In evaluating derivatives of the action, we follow the rule that derivatives with respect to $C^\phi(t_1, t_2)$ also affect $C^\phi(t_2, t_1)$, and likewise for $\hat{C}^\phi(t_1, t_2)$, due to the symmetry in the action. Using the vanishing of correlation functions involving only the

conjugate field $\hat{x}(t)$, the saddle-point conditions yield

$$\hat{C}_\star^\phi(t_1, t_2) = 0, \quad (41)$$

$$C_\star^\phi(t_1, t_2) = \langle \phi(t_1)\phi(t_2) \rangle_\star, \quad (42)$$

where $\langle \dots \rangle_\star$ denotes an average within the dynamic process described by $W[C_\star^\phi, 0]$. This recovers the same single-site process (Eq. 17, Eq. 18) and self-consistency condition (Eq. 19) described in Sec. II C.

C. Four-point functions

We now compute $\Psi_\star^a(\boldsymbol{\tau})$ within the path-integral formalism. Fluctuations around the saddle point derived above are governed by the Hessian of the action [40, 59]. This Hessian has blocks given by

$$H_{C^\phi C^\phi}(t_1, t_2, t_3, t_4) = \frac{\delta^2 S}{\delta C^\phi(t_1, t_2)\delta C^\phi(t_3, t_4)} = -g^4 \langle \langle \hat{x}(t_1)\hat{x}(t_2), \hat{x}(t_3)\hat{x}(t_4) \rangle \rangle_\star, \quad (43a)$$

$$H_{C^\phi \hat{C}^\phi}(t_1, t_2, t_3, t_4) = \frac{\delta^2 S}{\delta C^\phi(t_1, t_2)\delta \hat{C}^\phi(t_3, t_4)} = -I(t_1, t_2, t_3, t_4) - g^2 \langle \langle \hat{x}(t_1)\hat{x}(t_2), \phi(t_3)\phi(t_4) \rangle \rangle_\star, \quad (43b)$$

$$H_{\hat{C}^\phi \hat{C}^\phi}(t_1, t_2, t_3, t_4) = \frac{\delta^2 S}{\delta \hat{C}^\phi(t_1, t_2)\delta \hat{C}^\phi(t_3, t_4)} = -\langle \langle \phi(t_1)\phi(t_2), \phi(t_3)\phi(t_4) \rangle \rangle_\star, \quad (43c)$$

where $\langle \langle A, B \rangle \rangle_\star = \langle AB \rangle_\star - \langle A \rangle_\star \langle B \rangle_\star$, $I(t_1, t_2, t_3, t_4) = \delta(t_1 - t_3)\delta(t_2 - t_4) + \delta(t_1 - t_4)\delta(t_2 - t_3)$. Expanding the action to second order around the saddle point, the path integral becomes

$$Z = \exp(-N\mathcal{S}[C_\star^\phi, 0]) \int \mathcal{D}\delta C^\phi \mathcal{D}\delta \hat{C}^\phi \quad (44)$$

$$\times \exp\left(-\frac{N}{2} \begin{pmatrix} \delta C^\phi \\ \delta \hat{C}^\phi \end{pmatrix}^T \begin{pmatrix} H_{C^\phi C^\phi} & H_{C^\phi \hat{C}^\phi} \\ H_{\hat{C}^\phi C^\phi}^T & H_{\hat{C}^\phi \hat{C}^\phi} \end{pmatrix} \begin{pmatrix} \delta C^\phi \\ \delta \hat{C}^\phi \end{pmatrix}\right),$$

revealing the structure of the Gaussian fluctuations around the saddle point. The covariance matrix among the fluctuation variables, $\delta C^\phi(t_1, t_2)$ and $\delta \hat{C}^\phi(t_1, t_2)$, is $1/N$ times the inverse Hessian, yielding

$$N \langle \delta C^\phi(t_1, t_2)\delta C^\phi(t_3, t_4) \rangle_\star \quad (45)$$

$$= \left[H_{C^\phi C^\phi} - H_{C^\phi \hat{C}^\phi} H_{\hat{C}^\phi \hat{C}^\phi}^{-1} H_{\hat{C}^\phi C^\phi} \right]^{-1}(t_1, t_2, t_3, t_4).$$

In principle, we have all the necessary components to evaluate this expression: the single-site dynamics are known via the saddle-point condition, and the Hessian blocks are given in terms of connected correlation functions in this single-site process. We could then take the temporal separation limits of Eq. 34 to obtain $\Psi_\star^\phi(\boldsymbol{\tau})$. The challenge is that each Hessian block is a complicated time²-by-time² matrix that, for general values of the time variables, has no analytic inverse. To circumvent this problem, we show in Appendix C that the temporal limits of Eq. 34 can be taken *before* taking the inverses. Under these temporal

limits, the Hessian blocks are

$$H_{\hat{C}^\phi \hat{C}^\phi}(t_1, t_2, t_3, t_4) = -C_\star^\phi(\tau_1)C_\star^\phi(\tau_2), \quad (46)$$

$$H_{C^\phi \hat{C}^\phi}(t_1, t_2, t_3, t_4) \quad (47)$$

$$= -\delta(\tau_1)\delta(\tau_2) + g^2 S_\star^\phi(-\tau_1)S_\star^\phi(-\tau_2),$$

$$H_{C^\phi C^\phi}(t_1, t_2, t_3, t_4) = 0, \quad (48)$$

where we used the fact that multiplication by $-i\hat{x}(t)$ is equivalent to a functional derivative with respect to a source at time t . Since the relevant quantities are now translation-invariant, i.e., depend only on τ_1 and τ_2 , we can transform to Fourier space. In this representation, each Hessian block becomes a frequency-dependent scalar,

$$H_{\hat{C}^\phi \hat{C}^\phi}(\boldsymbol{\omega}) = -C_\star^\phi(\omega_1)C_\star^\phi(\omega_2), \quad (49)$$

$$H_{C^\phi \hat{C}^\phi}(\boldsymbol{\omega}) = -1 + g^2 (S_\star^\phi(\omega_1)S_\star^\phi(\omega_2))^*, \quad (50)$$

$$H_{C^\phi C^\phi}(\boldsymbol{\omega}) = 0. \quad (51)$$

In summary, the full Hessian can be replaced by a two-by-two, frequency-dependent Hessian given by

$$\mathbf{H} = \begin{pmatrix} 0 & -1 + g^2(S_{12}^\phi)^* \\ -1 + g^2 S_{12}^\phi & -C_{12}^\phi \end{pmatrix}, \quad (52)$$

where we simplified notation by suppressing frequency arguments via the shorthand $C_{12}^\phi = C_\star^\phi(\omega_1)C_\star^\phi(\omega_2)$ and $S_{12}^\phi = S_\star^\phi(\omega_1)S_\star^\phi(\omega_2)$. The Fourier-space function $\Psi_\star^\phi(\boldsymbol{\omega})$ is the upper-left element of the inverse of this matrix. Performing the two-by-two matrix inversion gives

$$\Psi_\star^\phi = \frac{C_{12}^\phi}{|1 - g^2 S_{12}^\phi|^2}, \quad (53)$$

which agrees with the two-site cavity result (Eq. 20).

To summarize, we compute $\Psi_\star^\phi(\boldsymbol{\tau})$ through the following steps (in the next section, we show how to compute $\Psi_\star^x(\boldsymbol{\tau})$):

1. Write down the path integral, integrate out disorder, and introduce two-point fields and conjugate partners to factorize the action along extensive indices.
2. Solve the saddle-point equations of the resulting action, yielding the covariance and response functions.
3. Derive the frequency-dependent Hessian by computing second derivatives of the action with respect to the two-point fields, applying the temporal limits of Eq. 34, and transforming to Fourier space. Then, determine the element of the inverse frequency-dependent Hessian corresponding to $\Psi_\star^\phi(\boldsymbol{\omega})$.

This approach allows for the efficient calculation of two- and four-point functions for a given model, requiring only a few lines of computation directly from the action of the theory. To demonstrate the flexibility of the path-integral approach in computing $\Psi_\star^a(\boldsymbol{\tau})$, we apply it to compute $\Psi_\star^\phi(\boldsymbol{\tau})$ for a generalization of the i.i.d. model in which there are correlations between reciprocal couplings, recovering the result in [25] from the two-site cavity method (Appendix E).

D. Adding sources

Above, computing $\Psi_\star^\phi(\boldsymbol{\tau})$ was simplified by $C^\phi(t_1, t_2)$ appearing naturally in the statistical field theory resulting from integrating out \boldsymbol{J} . To compute $\Psi_\star^x(\boldsymbol{\tau})$, we need to introduce a source-field term in the action.

Consider a general intensive action $\mathcal{S}[\boldsymbol{C}; \mathcal{J}]$ where \boldsymbol{C} is a collection of fields (e.g., $\boldsymbol{C} = \{C^\phi, \hat{C}^\phi\}$), and \mathcal{J} is a source. In Appendix D, we show that

$$\begin{aligned} & \frac{\delta^2}{\delta \mathcal{J}^2} \log Z \Big|_{\mathcal{J}=0} \\ &= \left[-\frac{\delta^2 S}{\delta \mathcal{J}^2} + \left(\frac{\delta^2 S}{\delta \mathcal{J} \delta \boldsymbol{C}} \right)^T \boldsymbol{H}^{-1} \frac{\delta^2 S}{\delta \mathcal{J} \delta \boldsymbol{C}} \right]_{\mathcal{J}=0}, \end{aligned} \quad (54)$$

with all quantities evaluated at the saddle point. By applying this formula to the action of the i.i.d. model with the source term $-\frac{1}{2}x\mathcal{J}x$ added to the single-site path integral

(Eq. 38), we recover the expression for $\Psi_\star^x(\boldsymbol{\tau})$ from the two-site cavity method (Clark *et al.* [25]; Eq. 21). For actions of the form $\mathcal{S}[\boldsymbol{C}; \mathcal{J}] = -\mathcal{J}C_a + \mathcal{J}$ -independent terms, this formula reduces to $(\delta^2/\delta \mathcal{J}^2) \log Z|_{\mathcal{J}=0} = [\boldsymbol{H}^{-1}]_{aa}$, as expected.

E. Path-integral analysis of the random-mode model

Having demonstrated the path-integral approach to computing two- and four-point functions in well known connectivity models, we now apply this formalism to the random-mode model. In terms of the mode matrices \boldsymbol{L} and \boldsymbol{R} , the path integral is

$$\begin{aligned} Z[\boldsymbol{L}, \boldsymbol{R}] &= \int \mathcal{D}\boldsymbol{x} \int \mathcal{D}\hat{\boldsymbol{x}} \\ &\times \exp \left(i \sum_i \hat{x}_i T[x_i] - i \sum_{i,j} [\boldsymbol{LDR}]_{ij} \hat{x}_i \phi_j \right). \end{aligned} \quad (55)$$

We would like to integrate out \boldsymbol{L} and \boldsymbol{R} , but this is complicated by them appearing together in a quadratic term in the action. To simplify the integration, we introduce a set of M latent variables,

$$z_a(t) = D_a \sum_i R_{ia} \phi_i(t), \quad (56)$$

and their conjugates $\hat{z}_a(t)$. We use indices i, j for neurons and a, b for latent variables. The introduction of these latent variables makes the action linear in \boldsymbol{L} and \boldsymbol{R} :

$$\begin{aligned} Z[\boldsymbol{L}, \boldsymbol{R}] &= \int \mathcal{D}\boldsymbol{x} \int \mathcal{D}\hat{\boldsymbol{x}} \int \mathcal{D}\boldsymbol{z} \int \mathcal{D}\hat{\boldsymbol{z}} \\ &\times \exp \left(i \sum_i \hat{x}_i T[x_i] + i \sum_a z_a \hat{z}_a \right. \\ &\quad \left. - i \sum_{i,a} L_{ia} \hat{x}_i z_a - i \sum_{i,a} D_a R_{ia} \phi_i \hat{z}_a \right). \end{aligned} \quad (57)$$

We can now easily integrate out \boldsymbol{L} and \boldsymbol{R} . To factorize the action over indices spanning extensive dimensions, we introduce the field $C^\phi(t_1, t_2)$ (Eq. 5) with conjugate $\hat{Q}(t_1, t_2)$ as well as

$$Q(t_1, t_2) = \frac{1}{M} \sum_a z_a(t_1) z_a(t_2) \quad (58)$$

with conjugate $\hat{C}^\phi(t_1, t_2)$. The disorder-averaged path integral is

$$Z = \int \mathcal{D}C^\phi \int \mathcal{D}\hat{C}^\phi \int \mathcal{D}Q \int \mathcal{D}\hat{Q} \exp\left(-NS[C^\phi, \hat{C}^\phi, Q, \hat{Q}]\right), \quad (59)$$

$$\mathcal{S}[C^\phi, \hat{C}^\phi, Q, \hat{Q}] = -\frac{1}{2}C^\phi \hat{Q} - \frac{1}{2}Q \hat{C}^\phi - \log W^x[Q, \hat{Q}] - \alpha \left\langle \log W_D^z[C^\phi, \hat{C}^\phi] \right\rangle_D, \quad (60)$$

$$W^x[Q, \hat{Q}] = \int \mathcal{D}x \int \mathcal{D}\hat{x} \exp\left(i\hat{x}T[x] - \frac{1}{2}\phi\hat{Q}\phi - \frac{1}{2}\hat{x}Q\hat{x}\right), \quad (61)$$

$$W_D^z[C^\phi, \hat{C}^\phi] = \int \mathcal{D}z \int \mathcal{D}\hat{z} \exp\left(i\hat{z}z - \frac{1}{2}z\hat{C}^\phi z - \frac{1}{2}D^2\hat{z}C^\phi\hat{z}\right). \quad (62)$$

Thus, analysis of the path integral is made tractable by recasting the problem as interacting neurons and latent variables. The neuronal single-site picture is described by $W^x[Q, \hat{Q}]$, and the latent-variable single-site picture is described by $W_D^z[C^\phi, \hat{C}^\phi]$, where the subscript D reflects that each latent variable has its own component strength. This formulation introduces an extensive set of latent variables $z_a(t)$, in contrast to the finite set of latent variables, conventionally denoted by $\kappa_a(t)$, in low-rank neural networks [30, 31]. The statistics of the Gaussian input to each single-site process (neurons or latent variables) are determined by the statistics of the other process, creating a bipartite, mutually referential structure that also arises in the cavity treatment of the problem.

1. Two-point functions

Following the steps outlined at the end of Sec. III C, we first compute the DMFT by calculating the saddle point. The derivatives of the action are

$$\frac{\delta\mathcal{S}}{\delta C^\phi(t_1, t_2)} = -\hat{Q}^\phi(t_1, t_2) + \alpha \left\langle D^2 \langle \hat{z}(t_1)\hat{z}(t_2) \rangle_{W_D^z} \right\rangle_D, \quad (63)$$

$$\frac{\delta\mathcal{S}}{\delta \hat{C}^\phi(t_1, t_2)} = -Q(t_1, t_2) + \alpha \left\langle \langle z(t_1)z(t_2) \rangle_{W_D^z} \right\rangle_D, \quad (64)$$

$$\frac{\delta\mathcal{S}}{\delta Q(t_1, t_2)} = -\hat{C}^\phi(t_1, t_2) + \langle \hat{x}(t_1)\hat{x}(t_2) \rangle_{W^x}, \quad (65)$$

$$\frac{\delta\mathcal{S}}{\delta \hat{Q}(t_1, t_2)} = -C^\phi(t_1, t_2) + \langle \phi(t_1)\phi(t_2) \rangle_{W^x}, \quad (66)$$

where $\langle \dots \rangle_{W^x}$ and $\langle \dots \rangle_{W_D^z}$ are averages within the dynamic processes described by $W^x[Q, \hat{Q}]$ and $W_D^z[C^\phi, \hat{C}^\phi]$, respectively. Setting these derivatives to zero yields

$$\hat{C}_\star^\phi(t_1, t_2) = \hat{Q}_\star(t_1, t_2) = 0, \quad (67)$$

$$C_\star^\phi(t_1, t_2) = \langle \phi(t_1)\phi(t_2) \rangle_\star, \quad (68)$$

$$Q_\star(t_1, t_2) = \alpha \langle \langle z(t_1)z(t_2) \rangle_{\star D} \rangle_D, \quad (69)$$

where $\langle \dots \rangle_\star$ and $\langle \dots \rangle_{\star D}$ are averages within the dynamic processes described by $W^x[Q_\star, 0]$ and $W_D^z[C_\star^\phi, 0]$, respec-

tively. These single-site processes are

$$T[x](t) = \eta^x(t), \quad (70)$$

$$z(t) = \eta^z(t), \quad (71)$$

where $\eta^x(t)$ and $\eta^z(t)$ are Gaussian fields,

$$\eta^x \sim \mathcal{GP}(0, Q_\star), \quad (72)$$

$$\eta^z \sim \mathcal{GP}(0, D^2 C_\star^\phi), \quad (73)$$

showing that the neuronal and latent-variable single-site processes have mutually referential statistics [60].

Solving for $Q_\star(t_1, t_2)$ by combining Eq. 69, Eq. 71, and Eq. 73, we obtain $Q_\star(t_1, t_2) = \alpha r_2 C_\star^\phi(t_1, t_2)$, with r_n defined by Eq. 25. Consolidating these results, the self-consistent problem that determines $C_\star^\phi(t_1, t_2)$ can be expressed purely in terms of this correlation function as

$$T[x](t) = \eta^x(t),$$

$$\eta^x \sim \mathcal{GP}(0, \alpha r_2 C_\star^\phi),$$

$$C_\star^\phi(t_1, t_2) = \langle \phi(t_1)\phi(t_2) \rangle_\star.$$

Comparing to Eqs. 17–19, we recover the self-consistent equations of the i.i.d. model with coupling strength

$$g_{\text{eff}} = \sqrt{\alpha r_2}. \quad (74)$$

Thus, the low-rank coupling structure remains undetectable at the single-neuron level, where neurons experience effectively i.i.d. connections with variance g_{eff}^2/N . The structure of the random-mode model emerges only in collective neural activity, as we now demonstrate by calculating the four-point function.

2. Four-point functions

The frequency-dependent saddle-point Hessian is

$$\mathbf{H} = \left(\begin{array}{cc|cc} 0 & \alpha r_2 & 0 & -1 \\ \alpha r_2 & -\alpha r_4 C_{12}^\phi & -1 & 0 \\ \hline 0 & -1 & 0 & (S_{12}^\phi)^\star \\ -1 & 0 & S_{12}^\phi & -C_{12}^\phi \end{array} \right). \quad (75)$$

The upper-left block, corresponding to the latent variables, is related to the Hessian of an i.i.d. network with linear dynamics and a heterogeneous distribution of single-neuron scale factors D_a ; the lower-right block, corresponding to the neurons, is related to the Hessian of an i.i.d. network of nonlinear neurons (Eq. 52). They are coupled through the simple off-diagonal blocks, reflecting the interaction between neurons and latent variables. Finally, we obtain for the four-point function:

$$\Psi_{\star}^{\phi} = \frac{1 + \frac{1}{\alpha \text{PR}^D} |g_{\text{eff}}^2 S_{12}^{\phi}|^2}{|1 - g_{\text{eff}}^2 S_{12}^{\phi}|^2} C_{12}^{\phi}. \quad (76)$$

To obtain Ψ_{\star}^x , we add $-\frac{1}{2}x\mathcal{J}x$ to the neuronal single-site path integral (Eq. 61) and compute

$$\frac{\delta^2 S}{\delta \mathcal{J}^2} = -C_{12}^x, \quad \frac{\delta^2 S}{\delta \mathcal{J} \delta \mathcal{C}} = \begin{pmatrix} 0 \\ 0 \\ S_{12}^x \\ -C_{12}^{x\phi} \end{pmatrix}. \quad (77)$$

Inserting these into Eq. 54 and using a formula (Eq. F1) to invert the Hessian, we obtain

$$\Psi_{\star}^x = C_{12}^x + \left(1 + \frac{1}{\alpha \text{PR}^D}\right) |U|^2 C_{12}^{\phi} + UC_{12}^{x\phi} + \text{h.c.}, \quad (78)$$

where $U = g_{\text{eff}}^2 S_{12}^x / (1 - g_{\text{eff}}^2 S_{12}^{\phi})$ (Eq. 21b with $g = g_{\text{eff}}$).

F. Interpreting the formulas

The analytic formulas for the four-point function of the random-mode model (Eq. 76 and Eq. 78) reveal several insights. Taking the limit $\alpha \text{PR}^D \rightarrow \infty$ for fixed g_{eff} , which leads to elements of \mathbf{J} being i.i.d., recovers the known formulas for i.i.d. couplings (Eq. 20 and Eq. 21). Comparing to the i.i.d. formulas, any structure beyond i.i.d. connectivity (i.e., $1/\alpha \text{PR}^D$ being finite) strictly *decreases* the dimension of activity.

Our analysis reveals two key statistical features of the connectivity that characterize how connectivity shapes activity: the effective coupling strength, g_{eff} , and the effective rank, αPR^D . The first characterizes the typical magnitude of couplings, while the second characterizes global information about the number of significant connectivity components. As in the i.i.d. model, g_{eff} influences both single-neuron activity (described by $C_{\star}^a(\tau)$) and collective activity (described by $\Psi_{\star}^a(\tau)$). In contrast, αPR^D influences collective activity exclusively. The random-mode model therefore provides independent control over single-neuron and collective aspects of activity.

To validate the theoretical prediction for $\Psi_{\star}^{\phi}(\tau)$ (Eq. 76), we simulated networks and computed the participation ratio from the empirical equal-time covariance matrix of the activations. For the component strengths

D_a , we used a spectrum given by

$$D_a \propto \exp(-\beta_D a/M) \quad (79)$$

for $a = 1, \dots, M$, which yields $\text{PR}^D = \beta_D^{-1} \tanh(\beta_D)$. The corresponding density is $P(D) = 1/\beta_D D$ with support on $[\exp(-\beta_D), 1]$. To attain a desired effective rank $\alpha \text{PR}^D < 1$, we set $\alpha = M/N = 1$ and solved for β . For $\alpha \text{PR}^D > 1$, we fixed $\text{PR}^D = 1$ and increased α . We adjusted g_{eff} by rescaling D_a (i.e., adjusting the proportionality constant in Eq. 79).

Our simulations show excellent agreement with theoretical predictions across parameter settings (Fig. 6). Fig. 6a illustrates how the dimension of activity, PR^{ϕ} , varies with αPR^D for different values of g_{eff} . Consistent with i.i.d.-coupling networks, PR^{ϕ} increases monotonically with g_{eff} [25]. It also increases monotonically with αPR^D , approaching the dimension of a network with i.i.d. couplings for large αPR^D (Fig. 6a inset). As αPR^D approaches zero, the dimension of activity also approaches zero. We examine the limits $g_{\text{eff}} \rightarrow 1^+$ and $\alpha \text{PR}^D \rightarrow 0$ in detail in Sec. IV.

Beyond the dimension of activity, which depends on $\Psi_{\star}^{\phi}(\tau)$ at $\tau = (0, 0)$, we also examined the temporal profile of this function. Fig. 6b shows a normalized version of $\Psi^{\phi}(\tau, 0)$, which is related to the correlation functions of leading principal components, for various values of g_{eff} and αPR^D . The decay timescale of $\Psi_{\star}^{\phi}(\tau, 0)$ decreases with increasing g_{eff} , approaching a limiting behavior at $g_{\text{eff}} \sim 10$. While αPR^D affects the overall scale of this function, and consequently the dimension of activity, it has little effect on the decay timescale, and thus little effect on the timescales of leading principal components (Fig. 6b, inset). Thus, the effective rank primarily influences the dimension of activity rather than the collective temporal structure.

IV. LIMITING BEHAVIOR OF THE RANDOM-MODE MODEL

Here we examine the behavior of the random-mode model in two limiting cases: as the system approaches the transition to chaos from above ($g_{\text{eff}} \rightarrow 1^+$), and in the limit of low effective rank ($\alpha \text{PR}^D \ll 1$).

We first consider approaching the transition to chaos from above, i.e., $g_{\text{eff}} \rightarrow 1^+$. The relevant expansion parameter is $g_{\text{eff}} - 1 \ll 1$. For networks with i.i.d. couplings, Clark *et al.* [25] showed that, for coupling strength g , $\Psi_{\star, \text{i.i.d.}}^a(\tau) \sim 1/(g-1)$ and $\text{PR}_{\text{i.i.d.}}^a \sim (g-1)^3$ in this limit. For the random-mode model, to leading order in $1/(g_{\text{eff}} - 1)$, we have

$$\Psi_{\star}^a(\tau) = \left(1 + \frac{1}{\alpha \text{PR}^D}\right) \underbrace{\Psi_{\star, \text{i.i.d.}}^a(\tau)}_{\sim 1/(g_{\text{eff}}-1)}. \quad (80)$$

Consequently, to leading order in $g_{\text{eff}} - 1$, the dimension

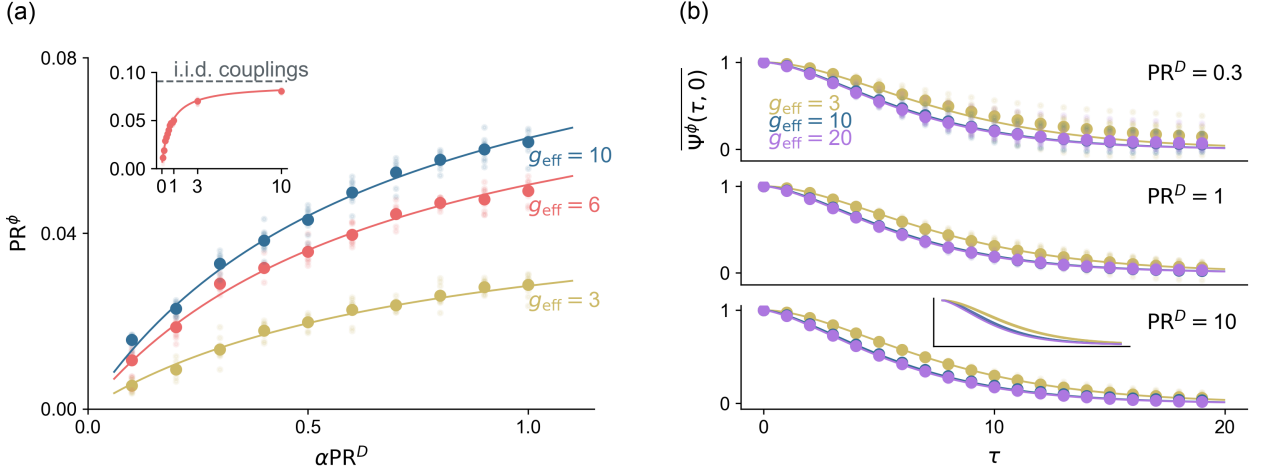


FIG. 6. Dimension of activity and collective timescales in the random-mode model. (a) Activity dimension PR^ϕ versus effective rank αPR^D for various coupling strengths g_{eff} . Thin dots: individual simulations; thick dots: means over 10 simulations; lines: theoretical predictions. Inset: Extended $g_{\text{eff}} = 6$ case, showing convergence to i.i.d. coupling behavior with growing α . (b) Normalized four-point function $\overline{\Psi}^\phi(\tau, 0) \equiv \Psi^\phi(\tau, 0)/\Psi^\phi(0, 0)$ for various g_{eff} and αPR^D . Inset: Theory curves for all αPR^D , demonstrating relative invariance of collective timescales to the effective rank. Simulations use $N = 5000$ neurons.

of activity behaves as

$$PR^a = \left(1 + \frac{1}{\alpha PR^D}\right)^{-1} \underbrace{PR_{\text{i.i.d.}}^a}_{\sim (g_{\text{eff}} - 1)^3}. \quad (81)$$

Thus, as the network approaches the transition to chaos, the effect of structure in connectivity is to reduce the dimension by a factor of $(1 + 1/\alpha PR^D)^{-1}$ compared to a network with i.i.d. couplings. Taking the further limit of $\alpha PR^D \ll 1$ yields the simple relation

$$PR^a = \alpha PR^D PR_{\text{i.i.d.}}^a. \quad (82)$$

The difference between αPR^D and PR^S is a higher-order correction, so we also have

$$PR^a = PR^S PR_{\text{i.i.d.}}^a. \quad (83)$$

That is, in the limits of both low effective rank and small effective coupling strength, the dimension of activity is equal to the dimension of the singular-value spectrum times the dimension of activity in an i.i.d. network.

We now consider the limit of low effective rank, $\alpha PR^D \ll 1$, for arbitrary g_{eff} . In this limit, the component strengths D_a closely approximate the singular values of the coupling matrix. To leading order in αPR^D ,

$$PR^a = K^a(g_{\text{eff}}) \alpha PR^D, \quad (84)$$

where

$$K^\phi(g_{\text{eff}}) = C_\star^\phi(0)^2 \left[\int d\omega \left| \frac{g_{\text{eff}}^2 S_{12}^\phi}{1 - g_{\text{eff}}^2 S_{12}^\phi} \right|^2 C_{12}^\phi \right]^{-1}, \quad (85)$$

$$K^x(g_{\text{eff}}) = C_\star^x(0)^2 \left[\int d\omega \left| \frac{g_{\text{eff}}^2 S_{12}^x}{1 - g_{\text{eff}}^2 S_{12}^x} \right|^2 C_{12}^\phi \right]^{-1}. \quad (86)$$

We match this theory of limiting behavior to simulated networks with $\alpha = 1$ and a step function for the component strengths:

$$D_a = \begin{cases} \text{const.} & \frac{a}{N} \leq PR^D \\ 0 & \frac{a}{N} > PR^D. \end{cases} \quad (87)$$

We varied PR^D and verified its linear relationships with PR^ϕ and PR^x in the $PR^D \rightarrow 0$ limit (Fig. 7a).

Focusing on $K^\phi(g_{\text{eff}})$, note that its expression (Eq. 85) resembles the formula for the dimension of activity in a i.i.d. network with coupling strength g_{eff} , but includes an additional factor $|g_{\text{eff}}^2 S_{12}^\phi|^2$ in the integral (compare to Eq. 20). Numerical evaluation of $K^\phi(g_{\text{eff}})$ shows that it approaches $PR_{\text{i.i.d.}}^\phi$ as $g_{\text{eff}} \rightarrow 1^+$ as expected from Eq. 82. As g_{eff} increases, $K^\phi(g_{\text{eff}})$ increases monotonically to approximately $1.53 PR_{\text{i.i.d.}}^\phi$ (Fig. 7a, inset). These results show that for networks with low effective rank, $PR^\phi \sim \alpha PR^D PR_{\text{i.i.d.}}^\phi$ up to an order-one fudge factor that becomes exactly one as $g_{\text{eff}} \rightarrow 1^+$.

We also investigated the relationship between the eigenvalues λ_i^a of $C_{ij}^a(0)$ and the component strengths D_a . In the low-effective-rank limit, the quantities PR^a and αPR^D computed from these spectra exhibit a linear relationship (with proportionality factor $K^a(g_{\text{eff}})$), implying

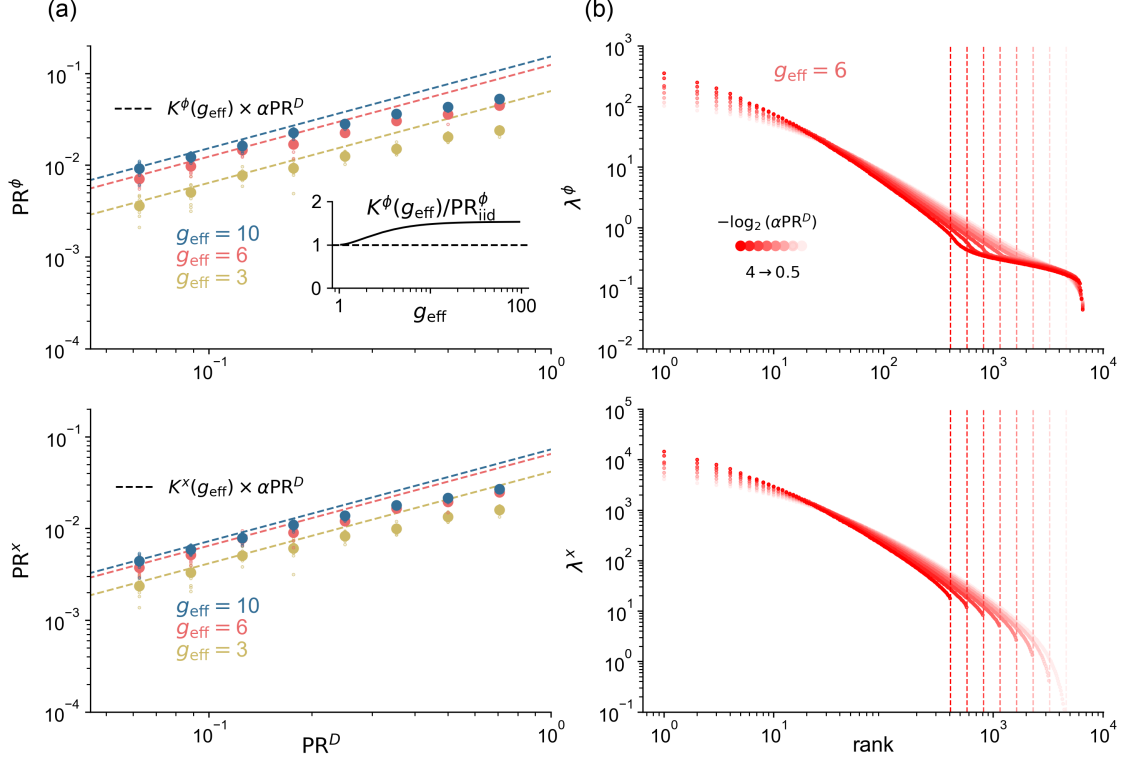


FIG. 7. Analysis of dimension of activity and covariance spectrum in the low-effective-rank limit. (a) Top: Dimension of activity PR^ϕ versus effective rank αPR^D ($\alpha = 1$) for various coupling strengths g_{eff} . Component strengths D_a are constant for $a/N \leq PR^D$ and 0 otherwise. Small dots: individual simulations; large dots: means over 10 simulations; solid lines: theoretical predictions; dotted lines: small- PR^D expansion, $K^\phi(g_{\text{eff}})PR^D$. Inset: Ratio of proportionality factor $K^\phi(g_{\text{eff}})$ to PR_{iid}^ϕ versus g_{eff} . Bottom: Same analysis for pre-activations. (b) Top: Rank-ordered eigenvalue plots for activation covariance matrix $C_{ij}^\phi(0)$. Dotted vertical lines indicate $N PR^D$. Bottom: Same for pre-activations. All simulations use $N = 6500$ neurons.

that the ratio of their second-squared and fourth moments are tightly linked. However, we find that the full forms of the eigenvalue and component-strength spectra differ markedly. Whereas the component strengths D_a decay according to a step function in this example, the rank-ordered eigenvalues λ^ϕ and λ^x decay smoothly (Fig. 7b). Thus, the dynamics transform the connectivity spectrum into an activity spectrum with a different form while preserving the linear relationship between PR^a and αPR^D .

V. CAVITY ANALYSIS OF THE RANDOM-MODE MODEL

While the path-integral approach provides a systematic framework for analyzing neural-network dynamics, the cavity method offers an intuitive, complementary perspective. This section provides an overview of the cavity analysis for the random-mode model, with the full mathematical details available in Appendix G. While these

approaches yield equivalent results, they differ in their methodology: the path-integral approach focuses on fluctuations around the saddle point in a field theory, whereas the cavity approach examines perturbations induced by a subset of held-out variables.

Leveraging Eq. 56, we reformulate the network as a bipartite system of neurons and latent variables and extend the cavity calculation of Clark *et al.* [25] to both groups. This leads to separate, mutually referential cavity pictures for each group, mirroring the two single-site path integrals (Sec. III E). As in the path-integral formalism, self-consistent expressions in one picture are defined using averages from the other. Unlike the path-integral approach, which derives $\Psi^\phi(\tau)$ using its time-by-time definition (Eq. 9), the cavity method derives this function using its neuron-by-neuron definition (Eq. 7).

The cavity method we employ, schematized in Fig. 8, has two key features that distinguish it from simpler cavity calculations. First, it uses a two-site structure: we consider the simultaneous removal of two neurons, or two latent variables, from the network, rather than just one.

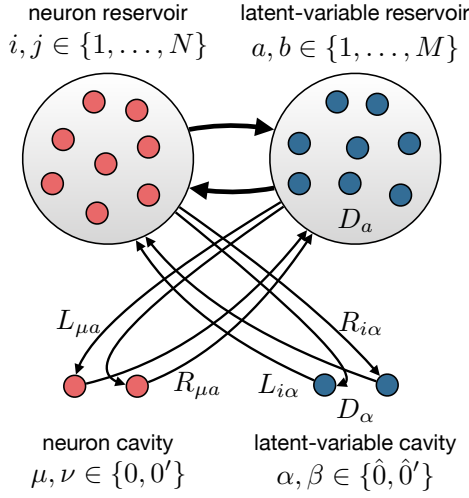


FIG. 8. Schematic of the two-site cavity approach for the bipartite representation of the random-mode model. Left: Neuron cavity, considering the introduction of neurons $x_0(t)$ and $x_{0'}(t)$. Right: Latent-variable cavity, considering the introduction of latent variables $z_0(t)$ and $z_{0'}(t)$. The cavity pictures are coupled, with averages from one appearing in self-consistent equations for the other.

This allows us to study pairwise correlations between neurons. This approach was previously used in Clark *et al.* [25]. Second, it incorporates a bipartite structure: we treat both neurons and latent variables as dynamic objects, creating separate but mutually referential cavity pictures for each group. Such bipartite structure, without the two-site structure, has been used in cavity calculations in the Hopfield model [61, 62]. Note that these two features are distinct: the two-site aspect refers to the number of neurons removed in each cavity, while the bipartite aspect refers to the types of variables considered (neurons and latent variables).

VI. SINGLE-NEURON HETEROGENEITY

While the random-mode model introduces heterogeneity in connectivity through the component strengths D_a , individual neurons may also exhibit heterogeneous properties. For instance, cortical neurons display a broad distribution of mean firing rates [63]. To compare the effects of low-dimensional structure in connectivity with the effects of heterogeneous neuronal properties, we extend our analysis to networks with diverse single-neuron characteristics.

In particular, we generalize the neuronal nonlinearity to $\Phi_{\theta}(x)$, which depends on a vector of parameters θ . The parameter vector for the i -th neuron, θ_i , is sampled i.i.d. from a distribution $P(\theta)$. This formulation allows us to model diverse neuronal properties such as gains or biases. When analyzing neural data, it is common to normalize neuronal activities (e.g., through z -scoring) to put them on the same scale. To facilitate analysis of

such normalized activations, we also introduce a set of variables $\phi_i(t) = \phi(x_i(t))$ that do not depend on θ_i .

We incorporate the generalized nonlinearity into the path integral, as well as a source term for the normalized variables, and integrate out \mathbf{L} and \mathbf{R} . To factorize the action over indices spanning extensive dimensions, we introduce, among others, the order parameter

$$C^{\Phi}(t_1, t_2) = \frac{1}{N} \sum_i \Phi_{\theta_i}(t_1) \Phi_{\theta_i}(t_2), \quad (88)$$

where $\Phi_{\theta_i}(t) = \Phi_{\theta_i}(x_i(t))$. In Appendix H, we derive a single-site dynamic process $T[x](t) = \eta^x(t)$, where $\eta^x \sim \mathcal{GP}(0, \alpha r_2 C_{\star}^{\Phi})$, with the self-consistency condition

$$C_{\star}^{\Phi}(t_1, t_2) = \langle \langle \Phi_{\theta}(t_1) \Phi_{\theta}(t_2) \rangle_{\star} \rangle_{\theta}. \quad (89)$$

This condition is identical to that of an i.i.d. network, but with an average over $\theta \sim P(\theta)$, in addition to the usual Gaussian average over $\eta^x(t)$, to account for single-neuron heterogeneity.

To write down the solution the solution for the four-point function, we define new two-frequency correlation functions with an outer average over $\theta \sim P(\theta)$:

$$\mathfrak{C}_{12}^{\Phi} = \langle \langle \Phi_{\theta} \Phi_{\theta} \rangle_{\star}(\omega_1) \langle \Phi_{\theta} \Phi_{\theta} \rangle_{\star}(\omega_2) \rangle_{\theta}, \quad (90a)$$

$$\mathfrak{s}_{12}^{\Phi} = \left\langle \left\langle \frac{\delta \Phi_{\theta}}{\delta I} \right\rangle_{\star}(\omega_1) \left\langle \frac{\delta \Phi_{\theta}}{\delta I} \right\rangle_{\star}(\omega_2) \right\rangle_{\theta}, \quad (90b)$$

$$\mathfrak{C}_{12}^{\Phi\phi} = \langle \langle \Phi_{\theta} \phi \rangle_{\star}(\omega_1) \langle \Phi_{\theta} \phi \rangle_{\star}(\omega_2) \rangle_{\theta}, \quad (90c)$$

along with the usual shorthand $C_{12}^{\Phi} = C_{\star}^{\Phi}(\omega_1) C_{\star}^{\Phi}(\omega_2)$. For the unnormalized variables $\Phi_{\theta_i}(t)$, we obtain

$$\Psi_{\star}^{\Phi} = \frac{\mathfrak{C}_{12}^{\Phi} + \frac{1}{\alpha \text{PR}^D} |\alpha r_2 \mathfrak{s}_{12}^{\Phi}|^2}{|1 - \alpha r_2 \mathfrak{s}_{12}^{\Phi}|^2} C_{12}^{\Phi}. \quad (91)$$

For the normalized variables $\phi_i(t)$, we obtain

$$\Psi_{\star}^{\phi} = \left[|A|^2 \left(\frac{\mathfrak{C}_{12}^{\phi}}{C_{12}^{\phi}} + \frac{1}{\alpha \text{PR}^D} \frac{C_{12}^{\phi}}{C_{12}^{\phi}} \right) + \left(A \frac{\mathfrak{C}_{12}^{\Phi\phi}}{C_{12}^{\phi}} + \text{h.c.} \right) + 1 \right] C_{12}^{\phi}, \quad (92)$$

where $A = \alpha r_2 S_{12}^{\phi} / (1 - \alpha r_2 \mathfrak{s}_{12}^{\phi})$.

A. Diverse single-neuron firing rates

An illustrative case of single-neuron heterogeneity occurs when the θ parameters consist of a gain parameter G_i for each neuron, modeling diversity in mean firing rates:

$$\Phi_{\theta_i}(x) = G_i \phi(x). \quad (93)$$

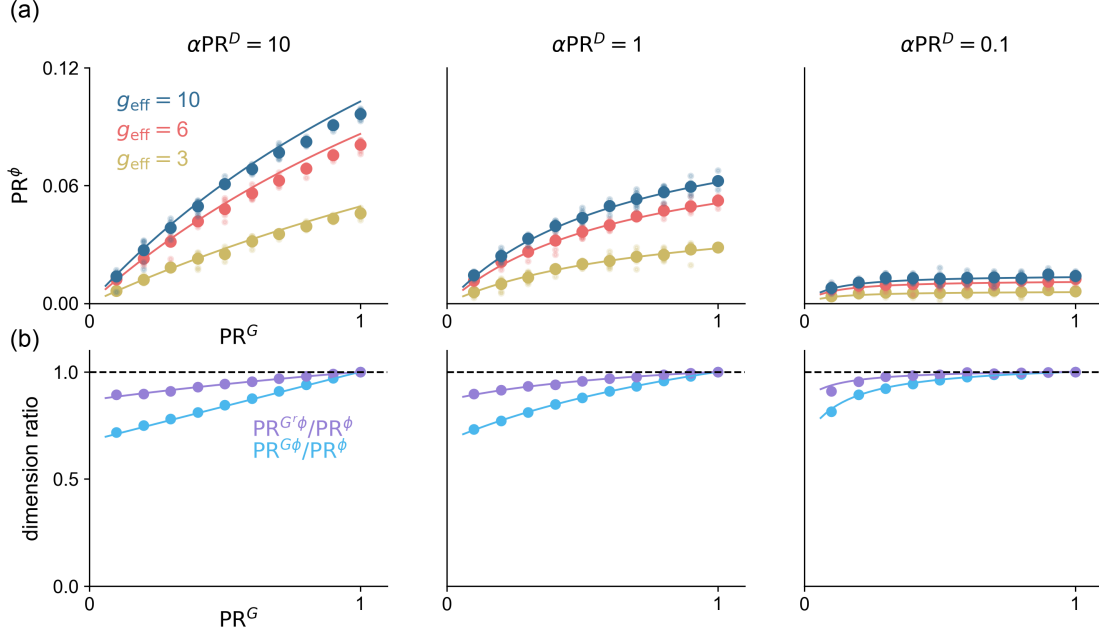


FIG. 9. Effect of single-neuron heterogeneity on dimension of activity in the random-mode model. (a) Dimension of normalized activity PR^ϕ versus participation ratio of gain distribution PR^G for various coupling strengths g_{eff} and effective ranks αPR^D . Thin dots: individual simulations; thick dots: means over 10 simulations; lines: theoretical predictions. (b) Fractional reduction in dimension for weighted activations relative to PR^ϕ . Blue: $G_i \phi_i$; purple: $G_i^{\text{readout}} \phi_i$. $g_{\text{eff}} = 10$. Thick dots: means over 10 simulations, averaging before taking the ratio; lines: theoretical predictions. All simulations use $N = 5000$ neurons.

In this scenario, the dynamics of the network are determined by an effective coupling matrix $\mathbf{LDR}^T \mathbf{G}$, where $\mathbf{G} = \text{diag}(G_1, \dots, G_N)$. This extension of the random-mode model allows us to directly compare the effects of low-dimensional structure in the connectivity (via the component strengths D_a) with heterogeneity in single-neuron properties (via the gains G_i). We assume the gains are drawn from a distribution with moments

$$q_n = \langle G^n \rangle_G. \quad (94)$$

To quantify the heterogeneity in firing rates, we define the participation ratio of the gain distribution:

$$PR^G = \frac{q_2^2}{q_4}. \quad (95)$$

We analyze collective activity for both the unnormalized activations $\Phi_{\theta_i}(t)$ and the normalized activations $\phi_i(t)$. The latter are analogous to z -scored firing rates in neural recordings, where z -scoring removes single-neuron heterogeneity while preserving nontrivial structure due to cross-neuron and temporal correlations.

For the unnormalized variables, we calculate the four-point function

$$\Psi_\star^\Phi = \frac{\frac{1}{PR^G} + \frac{1}{\alpha PR^D} |g_{\text{eff}}^2 S_{12}^\phi|^2}{|1 - g_{\text{eff}}^2 S_{12}^\phi|^2} C_{12}^\Phi, \quad (96)$$

and for the normalized variables,

$$\Psi_\star^\phi = \frac{1 + \left(\frac{1}{PR^G} + \frac{1}{\alpha PR^D} - 1\right) |g_{\text{eff}}^2 S_{12}^\phi|^2}{|1 - g_{\text{eff}}^2 S_{12}^\phi|^2} C_{12}^\phi, \quad (97)$$

where

$$g_{\text{eff}} = \sqrt{\alpha r_2 q_2}, \quad (98)$$

$$C_{12}^\Phi = q_2^2 C_{12}^\phi. \quad (99)$$

Eq. 97 demonstrates that reductions in effective rank, described by αPR^D , and in the heterogeneity of gains, described by PR^G , have symmetric effects on the dimension of normalized activity, with their combined effect captured by the harmonic mean, $\left(\frac{1}{\alpha PR^D} + \frac{1}{PR^G}\right)^{-1}$. This symmetry arises because swapping the distributions of D_a and G_i does not change the spectrum of $\mathbf{LDR}^T \mathbf{G}$ when \mathbf{L} and \mathbf{R} are i.i.d., since $\mathbf{LDR}^T \mathbf{G}$ and $\mathbf{R}^T \mathbf{G} \mathbf{L} \mathbf{D}$ have the same nonzero eigenvalues. One might expect that normalizing the activations before computing the dimension of activity would remove the effect of heterogeneous gains on the dimension. This is not the case, however, since neuronal gains affect the recurrent dynamics, and not merely the readout.

To further explore this and related effects, we compare the activity dimensions for three sets of activations: (1) unnormalized activations, $\Phi_{\theta_i}(t)$; (2) normalized activations, $\phi_i(t)$; and (3) normalized activations

multiplied by an independent set of “readout” gains, $\Phi_i^{\text{readout}}(t) = G_i^{\text{readout}}\phi_i(t)$, where the readout gains have the same distribution as the actual gains. Case (3) corresponds to variables with the same distribution of firing rates as the unnormalized activations, but where this heterogeneity is unrelated to the recurrent dynamics. In this case, we have $C_{12}^{\Phi^{\text{readout}}} = C_{12}^{\Phi} = q_2^2 C_{12}^{\phi}$. The four-point function is

$$\Psi^{\Phi^{\text{readout}}} = \left[\left(\frac{1}{\text{PR}^G} - 1 \right) \left(1 - g_{\text{eff}}^2 S_{12}^{\phi}|^2 + |g_{\text{eff}}^2 S_{12}^{\phi}|^2 \right) + 1 + \frac{1}{\alpha \text{PR}^D} |g_{\text{eff}}^2 S_{12}^{\phi}|^2 \right] \frac{C_{12}^{\Phi^{\text{readout}}}}{|1 - g_{\text{eff}}^2 S_{12}^{\phi}|^2}. \quad (100)$$

To validate our theoretical predictions (Eq. 96, Eq. 97, and Eq. 100), we simulated networks with component strengths and gains given by

$$D_a \propto \exp(-\beta_D a/M), \quad (101)$$

$$G_i \propto \exp(-\beta_G i/N). \quad (102)$$

The dimension of activity in these networks is determined by the coupling strength, g_{eff} ; the effective rank of the coupling matrix, αPR^D ; and the participation ratio of the single-neuron gain distribution, PR^G . Increases in each of these parameters leads to higher activity dimension for all three sets of activations.

Normalized activations consistently exhibit the highest dimension. While scaling normalized activations by heterogeneous factors reduces dimension as expected, the magnitude of this reduction depends on whether G_i or G_i^{readout} is used, even when their distributions are identical. This occurs because neurons with the largest gains preferentially participate in the leading modes of the normalized activations. Further scaling these already-dominant neurons by their gains results in overrepresentation of these neurons compared to using random gains. Thus, the dimension of unnormalized activations is lowest, with the dimension of random-readout activations falling between those of the normalized and unnormalized activations. This effect demonstrates that shuffling the normalizations of recorded neural activities should increase the dimension if firing rates and input covariances are related to one another, as they are in recurrent networks. Not observing such an increase in dimension, on the other hand, would suggest that heterogeneity in firing rates is unrelated to input covariance.

VII. MODE OVERLAPS

Thus far, we have assumed that the matrices \mathbf{L} and \mathbf{R} are independent of each other. Under this assumption, the overlap $\mathbf{L}_a^T \mathbf{R}_b$ between input mode b and output mode a is a random, $\mathcal{O}(1/\sqrt{N})$ quantity. However, to implement computations, modes must interact, suggesting

that the coupling matrices of real neural circuits have larger, structured overlaps between input and output modes.

To examine interactions between different modes in a real neural circuit, we returned to the connectome of *Drosophila melanogaster*. We computed the overlap matrix between its right and left singular vectors, which correspond to the input and output modes, respectively. Rather than the unstructured, $\mathcal{O}(1/\sqrt{N})$ overlaps expected from i.i.d. random modes, we observe structured, large overlaps (Fig. 10a). These large overlaps are particularly pronounced near the diagonal of the overlap matrix (Fig. 10b).

Motivated by these observations, we now extend the random-mode model to incorporate structured overlaps between input and output modes. Specifically, we define \mathbf{L} and \mathbf{R} as zero-mean Gaussian matrices with the following covariance structure:

$$\langle L_{ia} L_{jb} \rangle = \delta_{ij} \delta_{ab} \frac{1}{N}, \quad (103)$$

$$\langle R_{ia} R_{jb} \rangle = \delta_{ij} \delta_{ab} \frac{1}{N}, \quad (104)$$

$$\langle L_{ia} R_{jb} \rangle = \delta_{ij} \delta_{ab} \frac{O_{ab}}{N}, \quad (105)$$

where O_{ab} is the overlap matrix. In this case,

$$\langle \mathbf{L}^T \mathbf{R} \rangle = \mathbf{O}. \quad (106)$$

To capture the most salient feature of the fly connectome, large diagonal overlaps, we specialize to a diagonal form for the overlap matrix:

$$O_{ab} = \delta_{ab} \rho_a, \quad (107)$$

where ρ_a is the correlation between the a -th input and output modes. This form of the overlaps implies that, for large N , $\mathbf{L}_a^T \mathbf{R}_a = \rho_a$, while $\mathbf{L}_a^T \mathbf{R}_b$ for $a \neq b$ remains a random $\mathcal{O}(1/\sqrt{N})$ quantity. Incorporating this structure allows the random-mode model to more accurately match the eigenspectrum of the connectome, which has large outliers along the real axis (Fig. 10c).

Defining an instance of this connectivity with a well-defined large- N limit requires specifying a joint distribution from which (D_a, ρ_a) are sampled for each a . Our analytic expressions for the two- and four-point functions depend on averages $\langle \dots \rangle_{D, \rho}$ over this distribution. Note that for large N , self-connections (autapses) in \mathbf{J} are given by

$$J_{ii} = \alpha \langle D \rho \rangle_{D, \rho}, \quad (108)$$

which is, in general, $\mathcal{O}(1)$. To avoid biologically unrealistic strong self-connections, one can choose $\langle D \rho \rangle_{D, \rho} = 0$, in which case J_{ii} is random and $\mathcal{O}(1/\sqrt{N})$. Alternatively, if one interprets each model neuron as a cluster of biological neurons, strong self-connections can be interpreted as aggregated within-cluster connectivity [64, 65]. Further-

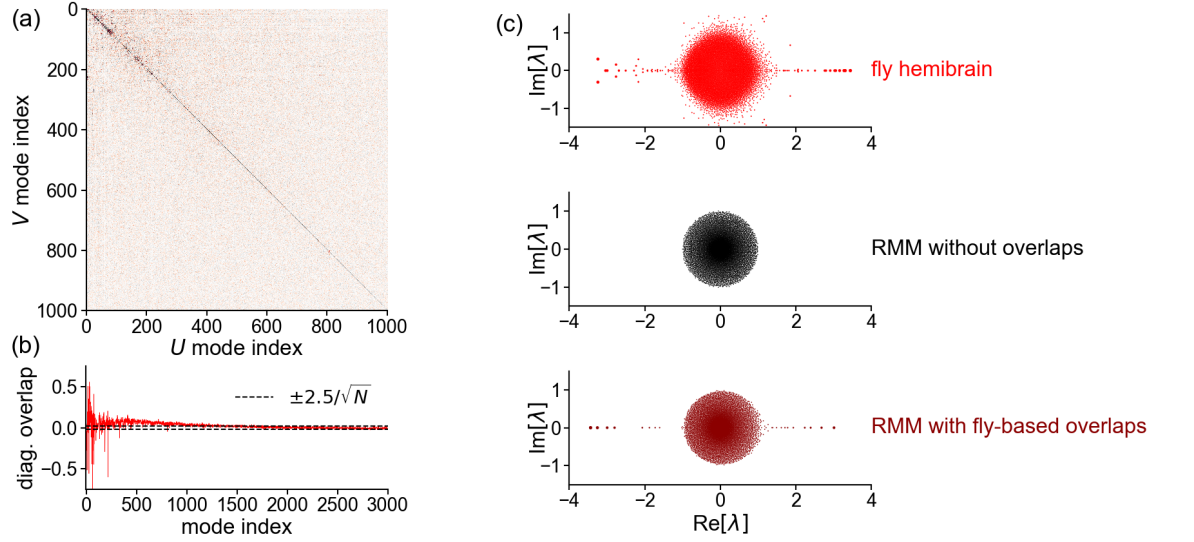


FIG. 10. Input-output mode overlaps and eigenvalue spectra of the fly-brain connectome. (a) Overlap matrix between right and left singular vectors of the connectome. First 1000 modes are shown. (b) First 3000 diagonal elements of the overlap matrix from (a). Horizontal lines indicate an approximate cutoff for $\mathcal{O}(1/\sqrt{N})$ random overlaps. (c) Eigenvalue spectra of various connectome-based matrices. Top: Actual hemibrain spectrum, exhibiting large outliers along the real axis. Middle: Eigenvalues from a realization of the random-mode model, using singular values from the connectome as component strengths D_a , resulting in a circularly symmetric spectrum. Bottom: Random-mode model realization with input-output mode overlaps incorporated, where overlaps are given by the inner products of left and right singular vectors from the fly-connectome SVD. Data from Scheffer *et al.* [21], $N = 18028$ neurons.

more, note that the covariance between reciprocal pairs of couplings is given by $N \langle J_{ij} J_{ji} \rangle_{\mathbf{J}} = \sigma$ ($i \neq j$) where

$$\sigma = \alpha \langle (D\rho)^2 \rangle_{D,\rho}. \quad (109)$$

We compute the two- and four-point functions using the path integral (Appendix I). As in previous cases, we obtain single-site processes for both neurons and latent variables. The neuronal single-site process is given by

$$T[x](t) = \eta^x(t) + [R_\star * \phi](t), \quad (110)$$

where $\eta^x \sim \mathcal{GP}(0, Q_\star)$ and $*$ denotes convolution. The input covariance $Q_\star(t_1, t_2)$ and convolutional kernel $R_\star(t_1, t_2)$ are defined in terms of statistics of the latent-variable single-site process. Due to the linearity of the latent-variable dynamics, we can express them as

$$Q_\star(\omega) = \alpha \left\langle \frac{D^2}{|1 - D\rho S_\star^\phi(\omega)|^2} \right\rangle_{D,\rho} C_\star^\phi(\omega), \quad (111)$$

$$R_\star(\omega) = \alpha \left\langle \frac{D\rho}{1 - D\rho S_\star^\phi(\omega)} \right\rangle_{D,\rho}. \quad (112)$$

We enforce $C_\star^\phi(t_1, t_2) = \langle \phi(t_1)\phi(t_2) \rangle_\star$ and $S_\star^\phi(t_1, t_2) = \langle \delta\phi(t_1)/\delta I(t_2) \rangle_\star$, yielding a self-consistent system that determines $C_\star^\phi(t_1, t_2)$ and $S_\star^\phi(t_1, t_2)$. Unlike previous cases, there is no effective coupling strength g_{eff} describing the relationship between $Q_\star(t_1, t_2)$ and $C_\star^\phi(t_1, t_2)$; instead,

this relationship involves a convolution with a kernel defined using the joint distribution over (D, ρ) . This can be viewed as a frequency-dependent effective coupling strength.

Expanding the self-coupling kernel $R_\star(\omega)$ (Eq. 112) in powers of ρ yields the first two terms

$$R_\star(\omega) = J_{ii} + \sigma S_\star^\phi(\omega) + \dots \quad (113)$$

The first term is what we get in the single-site picture for i.i.d. cross-neuron couplings and deterministic $\mathcal{O}(1)$ self couplings. The second term appears in the single-site picture if there are correlations between reciprocal pairs of couplings, but the structure is otherwise i.i.d. (Appendix E). Nonzero higher-order terms reflect that the structure of the random-mode model is not fully captured by either of these forms. Note that the first two terms being zero forces all subsequent terms to be zero. Thus, nonzero covariance among reciprocal pairs of couplings is a necessary and sufficient condition for attaining a nonzero self-coupling kernel in the single-site picture.

To compute the four-point function, we write down and

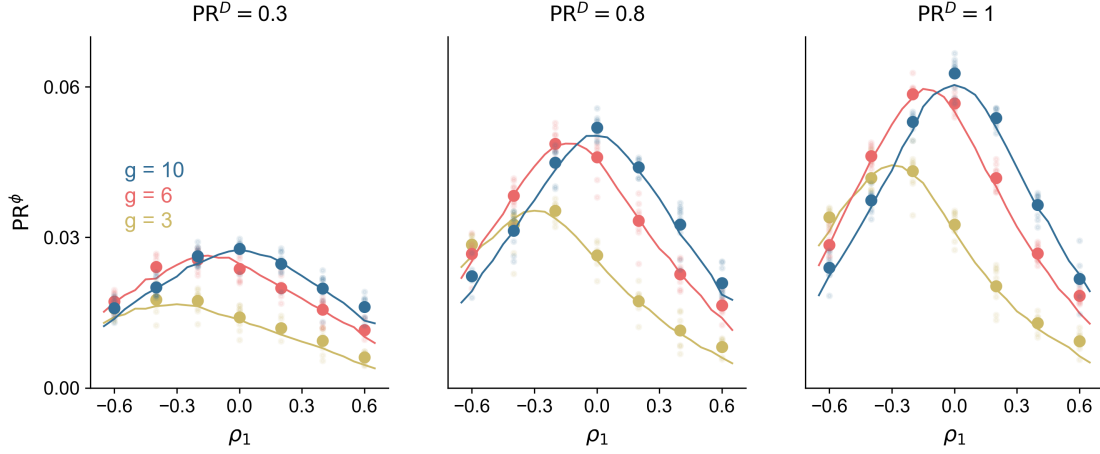


FIG. 11. Effect of input-output mode correlations on dimension of activity in the random-mode model. Dimension of activity PR^ϕ versus correlation parameter ρ_1 in the (D, ρ) joint distribution, for various coupling strengths g_{eff} and effective ranks αPR^D . Thin dots: individual simulations; thick dots: means over 10 simulations; lines: theoretical predictions. All simulations use $N = 5000$ neurons.

invert the frequency-dependent Hessian, and obtain

$$\Psi_\star^\phi = \frac{V - 1 + \left\{ \frac{(1+X_{12})(1+X_{21}^*)}{1-W^*} + \text{h.c.} \right\}}{|1-U|^2} C_{12}^\phi, \quad (114a)$$

$$U = \alpha \langle D^2 \Sigma_1 \Sigma_2 \rangle_{D,\rho}, \quad (114b)$$

$$V = \alpha \langle D^4 |\Sigma_1 \Sigma_2|^2 \rangle_{D,\rho}, \quad (114c)$$

$$W = \alpha \langle D^2 \rho^2 \Sigma_1^* \Sigma_2 \rangle_{D,\rho}, \quad (114d)$$

$$X_{12} = \alpha \langle D^3 \rho \Sigma_1 |\Sigma_2|^2 \rangle_{D,\rho}, \quad (114e)$$

$$\Sigma_k = \frac{S_k^\phi}{1 - D\rho S_k^\phi} \text{ for } k = 1, 2. \quad (114f)$$

We validated this theory by choosing parameterizations of D_a and ρ_a . We used $\alpha = M/N = 1$ and $D_a \propto \exp(-\beta_D a/N)$ for the component strengths, as before. For the overlaps ρ_a , we use a sigmoidal shape inspired by Fig. 10b in which the leading components have larger input-output mode overlaps. In particular, we used

$$\rho_a = \rho_1 \left(1 - \frac{2}{1 + \exp(-\beta_\rho (a/N - u_{\text{flip}}))} \right), \quad (115)$$

which varies from ρ_1 to $-\rho_1$, hitting $\rho_a = 0$ at $a/N = u_{\text{flip}}$. We fixed $\beta_\rho = 16$, varied ρ_1 , and set u_{flip} such that $\langle D\rho \rangle_{D,\rho} = 0$, eliminating strong self couplings. Across values of g_{eff} and PR^D , sufficiently strong overlaps of either sign reduce activity dimension (Fig. 11). The maximum dimension occurs for $\rho_1 < 0$, a regime in which activity projected along connectivity modes with the greatest strength is most strongly suppressed by the recurrent dynamics. This leftward shift is reduced for larger g_{eff} .

VIII. DISCUSSION

A key question in neuroscience and machine learning is how learning shapes collective dynamics through modifications of a neural network's connectivity. While our analysis has focused on disordered networks that generate chaotic activity and are not trained to perform tasks, the smooth low-rank connectivity structure we have explored provides a starting point for understanding the impact of learned coupling matrices on collective dynamics. Recent works have shown that large neural networks trained on real-world tasks exhibit smooth spectral structures in their coupling matrices, similar to those we have studied [20]. Moreover, while networks trained on simple tasks often display low-rank updates to their initial couplings, with a finite number of outlier eigenvalues emerging from the bulk [19, 46], training networks on many tasks, as is increasingly common, may produce coupling matrices with a low but extensive number of significant components [66, 67]. In such scenarios, the random-mode model, or extensions of it, may predict the resulting activity dimension and other aspects of collective dynamics. The path-integral formalism we have developed is also amenable to analyzing cases where the coupling matrix is drawn from a Gibbs ensemble with an energy function equal to the loss function for a task. This approach represents scenarios where couplings are trained to minimize a loss function with stochastic gradient descent [52]. Finally, initializing couplings with low-rank structure could improve training procedures like FORCE learning, which are based on suppressing chaos, because the initial strange attractor is lower-dimensional [11, 12].

Historically, neural connectivity was often characterized through network motifs – recurring patterns like cycles or chains among small neuronal groups [14, 68–70]. Such local statistics can be estimated using connectiv-

ity datasets obtained from methods that sample subsets of synapses. However, recent advances in whole-brain connectome reconstruction have unveiled global synaptic connectivity structures [71]. These connectomes reveal a more complex picture, where the spectrum and modes of the connectivity matrix exhibit large-scale structure that cannot be explained by local motifs [72]. Our parameterization of coupling matrices attempts to describe this global perspective, offering control over both the spectrum and mode overlaps. This could be particularly valuable in interpreting large-scale recordings of neural activity in the context of known anatomical connectivity.

In a similar vein, Tiberi *et al.* [72] proposed a random matrix theory approach for noise-driven linear networks based on parameterizing the eigendecomposition of \mathbf{J} . By contrast, our use of a DMFT approach allows us to describe nonlinear dynamics. Their parameterization also does not capture relationships between eigenvalues and eigenvectors, which are likely crucial for computations. Our parameterization, which is more akin to an SVD than an eigendecomposition, allows for a simultaneous parameterization of component strengths and corresponding mode overlaps. Other parameterizations of connectivity similar to the random-mode model have been used to study the relationship between spiking and rate-based recurrent networks [73] and to train spiking networks more efficiently [74].

Our description of single-neuron heterogeneity, where each neuron is parameterized by an arbitrary vector $\boldsymbol{\theta}$,

can be readily applied to explore how various forms of heterogeneity influence dimensionality and other features of collective activity. Introducing specific forms of heterogeneity constrained by observed electrophysiological properties [75] and other cell-specific characteristics across neurons could provide insight on the functional consequences of neuronal diversity [76].

On the technical side, we have demonstrated that the two-site cavity method and the analysis of fluctuations around the saddle point in the path integral approach yield equivalent results for computing the four-point function. This equivalence implies that the intricate cavity construction is equivalent to computing and inverting the Hessian of the action in the path integral. A deeper understanding of the relationship between these methods could lead to new hybrid approaches that combine the strengths of both techniques.

In conclusion, the random-mode model and associated analytical techniques provide a set of tools for exploring the relationship between connectivity and collective dynamics. Our parameterization of connectivity is a middle ground between deterministic low-rank models and completely random networks. Future work incorporating more complex mode interactions, diverse neuronal properties, and learning dynamics will further bridge neural connectivity, activity, and function.

ACKNOWLEDGEMENTS

We gratefully acknowledge L.F. Abbott for discussions and feedback on this work.

Appendix A: Glossary of Terms

Number of neurons (N):

Total number of neurons in the network.

Number of modes (M):

Number of components in the random-mode model.

(Effective) coupling strength (g, g_{eff}):

Standard deviation of the couplings times \sqrt{N} in the i.i.d. connectivity model (Eq. 14), random-mode model (Eq. 74), or variants thereof (Eq. 98).

Random-mode model:

Network connectivity model: $\mathbf{J} = \sum_{a=1}^M D_a \mathbf{L}_a \mathbf{R}_a^T$ (Eq. 22).

Connectivity component ($\mathbf{L}_a \mathbf{R}_a^T$):

Outer product of output and input modes.

Input mode (\mathbf{R}_a):

Neuronal pattern in the a -th component onto which activity patterns are projected.

Output mode (\mathbf{L}_a):

Neuronal pattern in the a -th component along which the projected activity pattern is expanded.

Component strength (D_a):

Scaling factor for the a -th component.

Ratio of modes to neurons (α):

Given by $\alpha = M/N$ (Eq. 24).

Participation ratio of component strengths (PR^D):

Given by $\text{PR}^D = r_2^2/r_4$ (Eq. 26) where $r_n = \langle D^n \rangle_D$ (Eq. 25).

Effective rank (αPR^D):

Connectivity dimensionality measure (Eq. 27).

Two-point function:

Correlation function given by $C^\phi(t_1, t_2) = \frac{1}{N} \sum_i \langle \phi_i(t_1) \phi_i(t_2) \rangle_t$ (Eq. 5).

Four-point function:

Higher-order correlation function given by $\Psi^\phi(\tau_1, \tau_2) = \frac{1}{N} \sum_{i,j} C_{ij}^\phi(\tau_1) C_{ij}^\phi(\tau_2)$ (Eq. 7). See also time-by-time definition (Eq. 9).

Appendix B: Preprocessing of the fly hemibrain connectome

We used the dataset originally presented in Scheffer *et al.* [21]. To form the connection matrix for analysis, we used synaptic counts as a measure of connection strength, determining the magnitudes of the matrix elements. Neurons were assigned neurotransmitter probabilities based on a machine-learning analysis applied to the electron-microscopy data [22]. We selected the most probable neurotransmitter assignment for each neuron. The neurotransmitter types were then mapped to signs (excitatory or inhibitory) according to Table I.

To normalize the connectivity matrix, we used an iterative scaling procedure analogous to the Sinkhorn–Knopp algorithm that proceeds as follows. We first rescale the positive elements in each row by a row-specific factor, such that the L2-norm of the positive elements is $1/\sqrt{2}$. The same procedure is applied to the negative elements, using a separate row-specific factor. This results in each row having a L2-norm of one with balanced excitatory and inhibitory inputs. A small number of neurons with exclusively excitatory or inhibitory inputs are left with an L2-norm of $1/\sqrt{2}$ instead of one. Following the row normalization, we perform the same operations on the columns. This disrupts the previous row normalization. Thus, we iterate the row and column normalization steps in an alternating fashion until convergence was achieved. The final result is a matrix with proper scaling along both rows and columns, which we interpret as the projection of the original matrix onto the set of properly row- and column-normalized matrices. Importantly, it has the same nonzero elements with the same signs as the original matrix.

Neurotransmitter	Synaptic Sign
GABA	-1 (Inhibitory)
Acetylcholine	+1 (Excitatory)
Glutamate	-1 (Inhibitory)
Serotonin	Ignored
Octopamine	Ignored
Dopamine	Ignored
Neither	Ignored

TABLE I. Mapping of neurotransmitters to synaptic signs

Appendix C: Temporal limits and inverses

Here, we demonstrate, for the i.i.d. model that the temporal limits in Eq. 34 can be taken before the inverses. This allows us to work with a frequency-dependent Hessian. In this section, we use Einstein notation for integrals over time variables (i.e., repeated time indices are integrated over). We would like to evaluate

$$\Psi(\tau_1, \tau_2) = U^{-1}(t_1, t_2, s_1, s_2) K(s_1, s_2, s_3, s_4) U^{-1}(t_1 + \tau_1, t_2 + \tau_2, s_3, s_4) \quad (\text{C1})$$

in the limits Eq. 34, where $U(t_1, t_2, t_3, t_4) = H_{\hat{C}\phi C\phi}(t_1, t_2, t_3, t_4)$ and $K(t_1, t_2, t_3, t_4) = H_{\hat{C}\phi \hat{C}\phi}(t_1, t_2, t_3, t_4)$ (note that $H_{C\phi C\phi}(t_1, t_2, t_3, t_4) = 0$ due to the vanishing of correlation functions involving only the conjugate field). Restating Eq. 43, we have

$$U(t_1, t_2, t_3, t_4) = -[\delta(t_1 - t_3)\delta(t_2 - t_4) + \delta(t_1 - t_4)\delta(t_2 - t_3)] - g^2 \langle \langle \phi(t_1)\phi(t_2), \hat{x}(t_3)\hat{x}(t_4) \rangle \rangle_\star, \quad (\text{C2})$$

$$K(t_1, t_2, t_3, t_4) = \langle \langle \phi(t_1)\phi(t_2), \phi(t_3)\phi(t_4) \rangle \rangle_\star. \quad (\text{C3})$$

We assume temporal stationarity throughout this section and consider only $a = \phi$.

We start by examining the properties of $U(t_1, t_2, t_3, t_4)$. U vanishes if one of the four time points is far (measured on the timescale of $C_\star^\phi(\tau)$) from the other three. For t_1 or t_2 , this is a consequence of the perturbation associated with $\hat{x}(t_1)$ or $\hat{x}(t_2)$ being far away; for t_3 or t_4 , this is a consequence of $\langle \phi(t_i) \rangle_\star = 0$ separating from the expectation. U also vanishes if there is more than one time point which is far from the remaining ones by the same arguments. Thus, the time points need to be close in pairs. However, if t_1, t_2 are close and t_3, t_4 are close, but the pairs are distant, U still vanishes since the perturbations associated with $\hat{x}(t_i)$ are both far. This leaves three possibilities for a non-vanishing U : t_1, t_3 close and t_2, t_4 close, but the pairs are distant; t_1, t_4 close and t_2, t_3 close, but the pairs are distant; or all time points are close.

Separating the three possibilities into two subdomains where all time points are close (c) and where the time points belong to either of the two pairwise separate (s) possibilities, we write $U = U_s + U_c$ where U_s and U_c are defined to vanish on the respective other domain. On the separated domain, U simplifies to

$$U_s(t_1, t_2, t_3, t_4) = -[\delta(t_1 - t_3)\delta(t_2 - t_4) + \delta(t_1 - t_4)\delta(t_2 - t_3)] + g^2 [S_\star^\phi(t_1 - t_3)S_\star^\phi(t_2 - t_4) + S_\star^\phi(t_1 - t_4)S_\star^\phi(t_2 - t_3)], \quad (\text{C4})$$

where we used that the two distant contributions are non-overlapping to add them.

We assume that we can also decompose the inverse into a contribution for separate pairs and a contribution where all time points are close, $U^{-1} = U_s^{-1} + U_c^{-1}$, where again U_s^{-1} and U_c^{-1} vanish on the respective other domain. We demonstrate that U_s^{-1} is the inverse of U_s , and that U_c^{-1} is the inverse of U_c , by noting that $U^{-1}(t_1, t_2, s_1, s_2)U(s_1, s_2, t_3, t_4)$ reduces to the contraction of U_c^{-1} and U_c if t_3 and t_4 , and hence s_1 and s_2 , are close; or to the contraction of U_s^{-1} and U_s if t_3 and t_4 , and hence s_1 and s_2 , are distant.

For Eq. C1, we need U_s^{-1} due to the limits Eq. 34. The fact that U reduces to U_s in the limits Eq. 34 justifies taking the limits before inverting U . Furthermore, these limits imply that, in Eq. C1, s_1 and s_2 , as well as s_3 and s_4 , are far apart. In this case, K simplifies to

$$K_s(s_1, s_2, s_3, s_4) = C_\star^\phi(s_1 - s_3)C_\star^\phi(s_2 - s_4) + C_\star^\phi(s_1 - s_4)C_\star^\phi(s_2 - s_3). \quad (\text{C5})$$

This justifies taking the limits Eq. 34 for K .

Appendix D: Incorporating sources

This section outlines the general approach for incorporating source terms and then applies it to the specific case of correlations among the pre-activations. Our goal is to compute

$$\left. \frac{\delta^2}{\delta \mathcal{J}^2} \log Z \right|_{\mathcal{J}=0}, \quad (\text{D1})$$

which gives the fluctuations around the mean of the quantity multiplying \mathcal{J} in the action. To facilitate this calculation, we introduce a new field U and set it equal to \mathcal{J} using the conjugate \hat{U} :

$$Z[\mathcal{J}] = \int \mathcal{D}\mathbf{C} \int \mathcal{D}U \int \mathcal{D}\hat{U} \exp\left(-N\hat{U}U + N\hat{U}\mathcal{J} - NS[\hat{\mathbf{C}}; U]\right). \quad (\text{D2})$$

Instead of taking the second derivative with respect to \mathcal{J} , we set $\mathcal{J} = 0$ and compute the fluctuations of \hat{U} in the augmented theory whose path integral is

$$Z = \int \mathcal{D}\mathbf{C} \int \mathcal{D}U \int \mathcal{D}\hat{U} \exp(-N\tilde{\mathcal{S}}[\mathbf{C}, U, \hat{U}]), \quad (\text{D3})$$

where

$$\tilde{\mathcal{S}}[\mathbf{C}, U, \hat{U}] = \hat{U}U + \mathcal{S}[\mathbf{C}; U]. \quad (\text{D4})$$

The Hessian of the augmented action, in terms of the Hessian of the original action, is

$$\left(\begin{array}{c|cc} \mathbf{H} & \frac{\partial^2 S}{\partial \mathcal{J} \partial \mathbf{C}} & \mathbf{0} \\ \hline \left(\frac{\partial^2 S}{\partial \mathcal{J} \partial \mathbf{C}} \right)^T & \frac{\partial^2 S}{\partial \mathcal{J}^2} & 1 \\ \mathbf{0}^T & 1 & 0 \end{array} \right), \quad (\text{D5})$$

where

$$H_{ab} = \frac{\delta^2 S}{\delta C_a \delta C_b}, \quad \left[\frac{\delta^2 S}{\delta \mathcal{J} \delta \mathbf{C}} \right]_a = \frac{\delta^2 S}{\delta \mathcal{J} \delta C_a}. \quad (\text{D6})$$

The fluctuations of \hat{U} are given by the bottom-right element of the inverse Hessian evaluated at the saddle point. Using a Schur complement to compute this element, we obtain the expression Eq. 54 stated in the main text.

We now apply Eq. 54 to the action of the i.i.d. connectivity model with a source term for correlations among pre-activations. The action is

$$\mathcal{S}[C^\phi, \hat{C}^\phi] = -\frac{1}{2} C^\phi \hat{C}^\phi - \log \int \mathcal{D}\mathbf{x} \int \mathcal{D}\hat{\mathbf{x}} \exp \left(i\hat{\mathbf{x}}T[\mathbf{x}] - \frac{g^2}{2} \hat{\mathbf{x}}C^\phi \hat{\mathbf{x}} - \frac{1}{2} \phi \hat{C}^\phi \phi - \frac{1}{2} \mathbf{x}\mathcal{J}\mathbf{x} \right). \quad (\text{D7})$$

Computing the necessary quantities and taking the temporal limits of Eq. 34, we obtain, in Fourier space,

$$\frac{\delta^2 S}{\delta \mathcal{J}^2} = -C_{12}^x, \quad \frac{\delta^2 S}{\delta \mathcal{J} \delta \mathbf{C}} = \begin{pmatrix} g^2 S_{12}^x \\ -C_{12}^{x\phi} \end{pmatrix}, \quad (\text{D8})$$

where $C_{12}^{x\phi} = C_\star^{x\phi}(\omega_1) C_\star^{x\phi}(\omega_2)$ and $S_{12}^x = S_\star^x(\omega_1) S_\star^x(\omega_2)$. Substituting these into Eq. 54 and using the frequency-dependent Hessian from Eq. 52, we obtain

$$\Psi_\star^x = C_{12}^x + |U|^2 C_{12}^\phi + U C_{12}^{x\phi} + \text{h.c.}, \quad \text{where } U = \frac{g^2 S_{12}^x}{1 - g^2 S_{12}^\phi}, \quad (\text{D9})$$

in agreement with the two-site cavity result of Clark *et al.* [25], given in Eq. 21.

Appendix E: Partially symmetric disorder

To demonstrate the flexibility of the path-integral approach to computing the four-point function, we now consider a generalization of the classic i.i.d. model in which we introduce correlations between reciprocal couplings, characterized by the following statistics:

$$\langle J_{ij} J_{kl} \rangle_{\mathbf{J}} = g^2 \delta_{ik} \delta_{jl} + g^2 \rho \delta_{il} \delta_{jk}. \quad (\text{E1})$$

Here, $\rho \in [-1, 1]$ is a parameter that controls the degree of symmetry in the connectivity. When $\rho = 1$, the connectivity is fully symmetric, while $\rho = -1$ corresponds to fully antisymmetric connectivity. The case $\rho = 0$ recovers the i.i.d. model. We express this partially symmetric connectivity as a linear combination of two matrices, \mathbf{X} and \mathbf{Y} , that are i.i.d. random with mean zero and variance $1/N$:

$$J_{ij} = \sqrt{g^2 - |\sigma|} X_{ij} + \sqrt{\frac{|\sigma|}{2}} (Y_{ij} + \text{sgn}(\sigma) Y_{ji}), \quad (\text{E2})$$

where $\sigma = \rho g^2$. In terms of \mathbf{X} and \mathbf{Y} , the path integral for this partially symmetric model is

$$Z[\mathbf{X}, \mathbf{Y}] = \int \mathcal{D}\mathbf{x} \int \mathcal{D}\hat{\mathbf{x}} \exp \left(i \sum_i \hat{x}_i T[x_i] - i \sqrt{g^2 - |\sigma|} \sum_{ij} X_{ij} \hat{x}_i \phi_j - i \sqrt{\frac{|\sigma|}{2}} \sum_{ij} Y_{ij} (\hat{x}_i \phi_j + \text{sgn}(\sigma) \phi_i \hat{x}_j) \right). \quad (\text{E3})$$

We integrate out \mathbf{X} and \mathbf{Y} . To factorize the action over indices spanning extensive dimensions, we introduce

$$C^\phi(t_1, t_2) = \frac{1}{N} \sum_i \phi_i(t_1) \phi_i(t_2), \quad \text{conjugate: } \hat{C}^\phi(t_1, t_2); \quad (\text{E4})$$

$$S^\phi(t_1, t_2) = \frac{1}{N} \sum_i \frac{\delta \phi_i(t_1)}{\delta I_i(t_2)}, \quad \text{conjugate: } \hat{S}^\phi(t_1, t_2). \quad (\text{E5})$$

We obtain, for the disorder-averaged path integral,

$$Z = \int \mathcal{D}C^\phi \int \mathcal{D}\hat{C}^\phi \int \mathcal{D}R \int \mathcal{D}\hat{R} \exp\left(-NS[C^\phi, \hat{C}^\phi, S^\phi, \hat{S}^\phi]\right), \quad (\text{E6})$$

$$\mathcal{S}[C^\phi, \hat{C}^\phi, S^\phi, \hat{S}^\phi] = -\frac{1}{2}C^\phi \hat{C}^\phi + \frac{\sigma}{2}S^\phi \hat{S}^\phi - \log W[C^\phi, \hat{C}^\phi, S^\phi, \hat{S}^\phi], \quad (\text{E7})$$

$$W[C^\phi, \hat{C}^\phi, S^\phi, \hat{S}^\phi] = \int \mathcal{D}\hat{x} \int \mathcal{D}x \exp\left(i\hat{x}T[x] - \frac{1}{2}\phi \hat{C}^\phi \phi - \frac{g^2}{2}\hat{x}C^\phi \hat{x} - \frac{i\sigma}{2}\phi \hat{S}^\phi \hat{x} - \frac{i\sigma}{2}\hat{x}S^\phi \phi\right). \quad (\text{E8})$$

To obtain the saddle-point solution, we compute the derivatives of the action, under the rule that derivatives with respect to $S^\phi(t_1, t_2)$ also affect $\hat{S}^\phi(t_2, t_1)$, and vice versa, due to the symmetry in the action. This gives

$$\frac{\delta \mathcal{S}}{\delta C^\phi(t_1, t_2)} = -\hat{C}^\phi(t_1, t_2) + g^2 \langle \hat{x}(t_1) \hat{x}(t_2) \rangle_W, \quad (\text{E9})$$

$$\frac{\delta \mathcal{S}}{\delta \hat{C}^\phi(t_1, t_2)} = -C^\phi(t_1, t_2) + \langle \phi(t_1) \phi(t_2) \rangle_W, \quad (\text{E10})$$

$$\frac{\delta \mathcal{S}}{\delta S^\phi(t_1, t_2)} = \sigma \hat{S}^\phi(t_1, t_2) + i\sigma \langle \hat{x}(t_1) \phi(t_2) \rangle_W, \quad (\text{E11})$$

$$\frac{\delta \mathcal{S}}{\delta \hat{S}^\phi(t_1, t_2)} = \sigma S^\phi(t_1, t_2) + i\sigma \langle \phi(t_1) \hat{x}(t_2) \rangle_W. \quad (\text{E12})$$

Setting these derivatives to zero yields the saddle-point conditions:

$$\hat{C}_\star^\phi(t_1, t_2) = 0, \quad (\text{E13})$$

$$C_\star^\phi(t_1, t_2) = \langle \phi(t_1) \phi(t_2) \rangle_\star, \quad (\text{E14})$$

$$S_\star^\phi(t_1, t_2) = \hat{S}_\star^\phi(t_2, t_1) = \left\langle \frac{\delta \phi(t_1)}{\delta I(t_2)} \right\rangle_\star, \quad (\text{E15})$$

where $\langle \dots \rangle_\star$ denotes an average within the dynamic process described by $W[C_\star^\phi, 0, S_\star^\phi, \hat{S}_\star^\phi]$. The single-site process at the saddle point is described by

$$T[x](t) = \eta^x(t) + \sigma [S_\star^\phi * \phi](t), \quad (\text{E16})$$

$$\eta^x \sim \mathcal{GP}(0, g^2 C_\star^\phi), \quad (\text{E17})$$

where $*$ denotes convolution. The symmetric structure provides a convolutional, nonlinear self-coupling $\sigma[S_\star^\phi * \phi](t)$ in the single-site dynamics. The two-point correlation and response functions, $C_\star^\phi(\tau)$ and $S_\star^\phi(\tau)$, must be determined self-consistently within this single site picture.

Introducing the notation $C_k^\phi = C_\star^\phi(\omega_k)$, $S_k^\phi = S_\star^\phi(\omega_k)$ for $k = 1, 2$, the frequency-dependent Hessian at the saddle point is

$$\mathbf{H} = \begin{pmatrix} 0 & -1 + g^2(S_{12}^\phi)^* & 0 & 0 \\ -1 + g^2 S_{12}^\phi & -C_{12}^\phi & \sigma S_1^\phi C_2^\phi & \sigma S_2^\phi C_1^\phi \\ 0 & \sigma(S_1^\phi)^* C_2^\phi & 0 & \sigma - \sigma^2(S_1^\phi)^* S_2^\phi \\ 0 & \sigma(S_2^\phi)^* C_1^\phi & \sigma - \sigma^2 S_1^\phi (S_2^\phi)^* & 0 \end{pmatrix}. \quad (\text{E18})$$

Inverting this matrix and isolating the upper-left element, we obtain, in agreement with Clark *et al.* [25],

$$\Psi_{\star}^{\phi} = \frac{1}{|1 - g^2 S_{12}^{\phi}|^2} \frac{1 - |\sigma(S_1^{\phi})^* S_2^{\phi}|^2}{|1 - \sigma(S_1^{\phi})^* S_2^{\phi}|^2} C_{12}^{\phi}. \quad (\text{E19})$$

Appendix F: Inverse formula

In Sec. III E 2 and Appendix H, we use the fact that

$$\begin{pmatrix} 0 & a^* & 0 & -1 \\ a & b & -1 & 0 \\ 0 & -1 & 0 & c^* \\ -1 & 0 & c & d \end{pmatrix}^{-1} = \begin{pmatrix} -\frac{b+|c|^2 d}{|1-ac|^2} & -\frac{c}{1-ac} & -\frac{a^* d+bc}{|1-ac|^2} & -\frac{1}{1-ac} \\ -\frac{c^*}{1-(ac)^*} & 0 & -\frac{1}{1-(ac)^*} & 0 \\ -\frac{ad+bc^*}{|1-ac|^2} & -\frac{1}{1-ac} & -\frac{|a|^2 d+b}{|1-ac|^2} & -\frac{a}{1-ac} \\ -\frac{1}{1-(ac)^*} & 0 & -\frac{a^*}{1-(ac)^*} & 0 \end{pmatrix}. \quad (\text{F1})$$

Appendix G: Two-site cavity calculation of the four-point function in the random-mode model

To apply cavity techniques, we reformulate the network as a bipartite system of neurons and latent variables,

$$T[x_i](t) = \sum_a L_{ia} z_a(t), \quad (\text{G1})$$

$$z_a(t) = D_a \sum_j R_{ja} \phi_j(t), \quad (\text{G2})$$

as done in the path-integral approach. In the two-site cavity calculation, we keep track various intermediate quantities to order $1/\sqrt{N}$, leading to an expression for $\Psi^{\phi}(\boldsymbol{\tau})$ accurate to leading order (order one), which we identify as $\Psi_{\star}^{\phi}(\boldsymbol{\tau})$.

To distinguish between different types of variables and their indices, we use the following notation. Neurons are indexed by $i, j \in \{1, \dots, N\}$ and latent variables by $a, b \in \{1, \dots, M\}$, as usual. For the cavity variables, we introduce special indices: neuronal cavity variables are indexed by $\mu, \nu \in \{0, 0'\}$, while latent cavity variables are indexed by $\alpha, \beta \in \{\hat{0}, \hat{0}'\}$.

1. Neuronal cavity

We begin by introducing two neurons, $x_0(t)$ and $x_{0'}(t)$. The leading-order ($1/\sqrt{N}$) effect on the latent variables is

$$\delta z_a(t) = \int^t dt' \sum_b S_{ab}^z(t_1, t_2) D_b \sum_{\mu} R_{\mu b} \phi_{\mu}(t'), \quad (\text{G3})$$

where $S_{ab}^z(t_1, t_2)$ is the response function of the latent variables. The dynamic equations for the cavity neurons are

$$T[x_{\mu}](t) = \eta_{\mu}(t) + \sum_{\nu} \int^t dt' F_{\mu\nu}(t_1, t_2) \phi_{\nu}(t'), \quad (\text{G4})$$

where

$$\eta_{\mu}(t) = \sum_a L_{\mu a} z_a(t), \quad (\text{G5})$$

$$F_{\mu\nu}(t_1, t_2) = \sqrt{N} \sum_{a,b} L_{\mu a} D_b R_{\nu b} S_{ab}^z(t_1, t_2). \quad (\text{G6})$$

Defining the cavity-field time-average cross-covariance as

$$C_{00'}^\eta(\omega) = \sum_{a,b} L_{0a} L_{0'b} C_{ab}^z(\omega), \quad (\text{G7})$$

we obtain the following expression for the cross-covariance of the cavity units, up to order $1/\sqrt{N}$:

$$C_{00'}^\phi(\omega) = |S_\star^\phi(\omega)|^2 C_{00'}^\eta(\omega) + \frac{1}{\sqrt{N}} [(S_\star^\phi(\omega) F_{00'}(\omega))^* + S_\star^\phi(\omega) F_{0'0}(\omega)] C_\star^\phi(\omega). \quad (\text{G8})$$

Our goal is to compute the parameter

$$\psi^\phi(\boldsymbol{\omega}) = N \left\langle C_{00'}^\phi(\omega_1) C_{00'}^\phi(\omega_2) \right\rangle_{\mathbf{L}, \mathbf{D}, \mathbf{R}}, \quad (\text{G9})$$

where $\langle \cdot \rangle_{\mathbf{L}, \mathbf{D}, \mathbf{R}}$ denotes an average over \mathbf{L} , \mathbf{D} , and \mathbf{R} . To evaluate this, we need to square and disorder-average [Eq. G8](#). This requires us to consider several two-frequency correlation functions, which we define as

$$\Gamma_{F_{00'}, F_{00'}}(\boldsymbol{\omega}) = \langle F_{00'}(\omega_1) F_{00'}(\omega_2) \rangle_{\mathbf{L}, \mathbf{D}, \mathbf{R}}, \quad (\text{G10})$$

$$\Gamma_{F_{00'}^*, F_{0'0}}(\boldsymbol{\omega}) = \langle F_{00'}^*(\omega_1) F_{0'0}(\omega_2) \rangle_{\mathbf{L}, \mathbf{D}, \mathbf{R}}, \quad (\text{G11})$$

$$\Gamma_{F_{00'}^*, C_{00'}^\eta}(\boldsymbol{\omega}) = \sqrt{N} \langle F_{00'}^*(\omega_1) C_{00'}^\eta(\omega_2) \rangle_{\mathbf{L}, \mathbf{D}, \mathbf{R}}, \quad (\text{G12})$$

$$\Gamma_{C_{00'}^\eta, C_{00'}^\eta}(\boldsymbol{\omega}) = N \langle C_{00'}^\eta(\omega_1) C_{00'}^\eta(\omega_2) \rangle_{\mathbf{L}, \mathbf{D}, \mathbf{R}}. \quad (\text{G13})$$

These have all been scaled to be order-one. We can evaluate these $\Gamma_{\dots}(\boldsymbol{\omega})$ functions due to the independence of the couplings and dynamic variables in the expressions defining them, which is a consequence of the cavity construction. Of these, the only nonvanishing ones are

$$\Gamma_{C_{00'}^\eta, C_{00'}^\eta}(\boldsymbol{\omega}) = \alpha \langle C_{\hat{0}\hat{0}}^z(\omega_1) C_{\hat{0}\hat{0}}^z(\omega_2) \rangle_{\mathbf{L}, \mathbf{D}, \mathbf{R}} + \alpha^2 N \langle C_{\hat{0}\hat{0}'}^z(\omega_1) C_{\hat{0}\hat{0}'}^z(\omega_2) \rangle_{\mathbf{L}, \mathbf{D}, \mathbf{R}}, \quad (\text{G14})$$

$$\Gamma_{F_{00'}, F_{00'}}(\boldsymbol{\omega}) = \alpha r_2 + \alpha^2 N \langle D_{\hat{0}'}^2 S_{\hat{0}\hat{0}'}^z(\omega_1) S_{\hat{0}\hat{0}'}^z(\omega_2) \rangle_{\mathbf{L}, \mathbf{D}, \mathbf{R}}, \quad (\text{G15})$$

where $\hat{0}, \hat{0}'$ denote the indices in the latent-variable cavity picture.

2. Latent-variable cavity

We now introduce two new latent variables, $z_{\hat{0}}(t)$ and $z_{\hat{0}'}(t)$. The leading-order ($1/\sqrt{N}$) effect on the neurons is

$$\delta\phi_i(t) = \int^t dt' \sum_j S_{ij}^\phi(t_1, t_2) \sum_\alpha L_{j\alpha} z_\alpha(t'), \quad (\text{G16})$$

where $S_{ij}^\phi(t_1, t_2)$ is the response function of the neurons. The dynamic equations for the cavity latent variables are

$$z_\alpha(t) = D_\alpha \left[\gamma_\alpha(t) + \frac{1}{\sqrt{N}} \sum_\beta \int^t dt' G_{\alpha\beta}(t_1, t_2) z_\beta(t') \right], \quad (\text{G17})$$

where

$$\gamma_\alpha(t) = \sum_i R_{i\alpha} \phi_i(t), \quad (\text{G18})$$

$$G_{\alpha\beta}(t_1, t_2) = \sqrt{N} \sum_{i,j} R_{i\alpha} L_{j\beta} S_{ij}^\phi(t_1, t_2). \quad (\text{G19})$$

Defining the time-average cavity-field cross-covariance as

$$C_{00'}^\gamma(\omega) = \sum_{i,j} R_{i0} R_{j0'} C_{ij}^\phi(\omega), \quad (\text{G20})$$

we obtain the following expression for the cross-covariance of the cavity latent variables up to order $1/\sqrt{N}$:

$$C_{00'}^z(\omega) = D_0 D_{0'} C_{00'}^\gamma(\omega) + \frac{1}{\sqrt{N}} [D_0 G_{00}^*(\omega) C_{0'0}^z(\omega) + D_{0'} G_{0'0}(\omega) C_{00}^z(\omega)]. \quad (\text{G21})$$

We aim to compute the parameter

$$\psi^z(\omega) = N \langle C_{00'}^z(\omega_1) C_{00'}^z(\omega_2) \rangle_{\mathbf{L}, \mathbf{D}, \mathbf{R}} \quad (\text{G22})$$

by squaring and disorder-averaging [Eq. G21](#). This requires us to consider several two-frequency correlation functions, which we define as

$$\Gamma_{G_{00'} G_{00'}}(\omega) = \langle G_{00'}(\omega_1) G_{00'}(\omega_2) \rangle_{\mathbf{D} \setminus \{D_0, D_{0'}\}}, \quad (\text{G23})$$

$$\Gamma_{G_{00'}^* G_{0'0}}(\omega) = \langle G_{00'}^*(\omega_1) G_{0'0}(\omega_2) \rangle_{\mathbf{D} \setminus \{D_0, D_{0'}\}}, \quad (\text{G24})$$

$$\Gamma_{G_{00'}^* C_{00'}^\gamma}(\omega) = \sqrt{N} \langle G_{00'}^*(\omega_1) C_{00'}^\gamma(\omega_2) \rangle_{\mathbf{D} \setminus \{D_0, D_{0'}\}}, \quad (\text{G25})$$

$$\Gamma_{C_{00'}^\gamma C_{00'}^\gamma}(\omega) = N \langle C_{00'}^\gamma(\omega_1) C_{00'}^\gamma(\omega_2) \rangle_{\mathbf{D} \setminus \{D_0, D_{0'}\}}. \quad (\text{G26})$$

Again, we can evaluate these $\Gamma_{\dots}(\omega)$ functions due to the independence of the couplings and dynamic variables in the expressions defining them. The nonvanishing ones are

$$\Gamma_{C_{00'}^\gamma C_{00'}^\gamma}(\omega) = C_\star^\phi(\omega_1) C_\star^\phi(\omega_2) + N \langle C_{00'}^\phi(\omega_1) C_{00'}^\phi(\omega_2) \rangle_{\mathbf{L}, \mathbf{D}, \mathbf{R}}, \quad (\text{G27})$$

$$\Gamma_{G_{00'} G_{00'}}(\omega) = S_\star^\phi(\omega_1) S_\star^\phi(\omega_2) + N \langle S_{00'}^\phi(\omega_1) S_{00'}^\phi(\omega_2) \rangle_{\mathbf{L}, \mathbf{D}, \mathbf{R}}, \quad (\text{G28})$$

where $0, 0'$ denote the indices in the neuronal cavity picture.

3. Combining the two two-site cavity pictures

To combine the results from both two-site cavity pictures, we use the following relations:

$$C_{00}^z(\omega) = D_0^2 C_\star^\phi(\omega), \quad (\text{G29})$$

$$S_{00'}^z(\omega) = \frac{D_0}{\sqrt{N}} G_{00'}(\omega), \quad (\text{G30})$$

$$S_{00'}^\phi(\omega) = \frac{1}{\sqrt{N}} (S_\star^\phi(\omega))^2 F_{00'}(\omega). \quad (\text{G31})$$

Using these relations and the definitions of the $\Gamma_{\dots}(\omega)$ functions (Eqs. [G10-G13](#) and [G23-G26](#)), we obtain

$$\Gamma_{C_{00'}^\eta C_{00'}^\eta}(\omega) = \alpha r_4 C_\star^\phi(\omega_1) C_\star^\phi(\omega_2) + \alpha^2 \psi^z(\omega), \quad (\text{G32})$$

$$\Gamma_{F_{00'} F_{00'}}(\omega) = \alpha r_2 [1 + \alpha r_2 \Gamma_{G_{00'} G_{00'}}(\omega)], \quad (\text{G33})$$

$$\Gamma_{C_{00'}^\gamma C_{00'}^\gamma}(\omega) = C_\star^\phi(\omega_1) C_\star^\phi(\omega_2) + \psi^\phi(\omega), \quad (\text{G34})$$

$$\Gamma_{G_{00'} G_{00'}}(\omega) = S_\star^\phi(\omega_1) S_\star^\phi(\omega_2) [1 + S_\star^\phi(\omega_1) S_\star^\phi(\omega_2) \Gamma_{F_{00'} F_{00'}}(\omega)]. \quad (\text{G35})$$

We solve Eq. G33 and Eq. G35 simultaneously, yielding

$$\Gamma_{F_{00'}F_{00'}}(\boldsymbol{\omega}) = \frac{\alpha r_2}{1 - \alpha r_2 S_{\star}^{\phi}(\omega_1) S_{\star}^{\phi}(\omega_2)}, \quad (\text{G36})$$

$$\Gamma_{G_{00'}G_{00'}}(\boldsymbol{\omega}) = \frac{S_{\star}^{\phi}(\omega_1) S_{\star}^{\phi}(\omega_2)}{1 - \alpha r_2 S_{\star}^{\phi}(\omega_1) S_{\star}^{\phi}(\omega_2)}. \quad (\text{G37})$$

With these solutions, we express $\psi_{\star}^z(\boldsymbol{\omega})$ and $\psi_{\star}^{\phi}(\boldsymbol{\omega})$ in terms of the $\Gamma \dots(\boldsymbol{\omega})$ functions. Switching to frequency-suppressed notation,

$$\psi_{\star}^z = r_2^2 \Gamma_{C_{00'}^{\gamma} C_{00'}^{\gamma}} + r_2 r_4 (\Gamma_{G_{00'}G_{00'}} + \text{h.c.}) C_{12}^{\phi}, \quad (\text{G38})$$

$$\psi_{\star}^{\phi} = |S_{12}^{\phi}|^2 \Gamma_{C_{00'}^{\eta} C_{00'}^{\eta}} + (\Gamma_{F_{00'}F_{00'}} S_{12}^{\phi} + \text{h.c.}) C_{12}^{\phi}. \quad (\text{G39})$$

Now, we substitute Eq. G38 into Eq. G39. Using $\Psi_{\star}^{\phi} = \psi_{\star}^{\phi} + C_{12}^{\phi}$, we obtain

$$\Psi_{\star}^{\phi} = |g_{\text{eff}}^2 S_{12}^{\phi}|^2 \left[\Psi_{\star}^{\phi} + \frac{1}{\alpha \text{PR}^D} \frac{1 - |g_{\text{eff}}^2 S_{12}^{\phi}|^2}{|1 - g_{\text{eff}}^2 S_{12}^{\phi}|^2} C_{12}^{\phi} \right] + \frac{1 - |g_{\text{eff}}^2 S_{12}^{\phi}|^2}{|1 - g_{\text{eff}}^2 S_{12}^{\phi}|^2} C_{12}^{\phi}, \quad (\text{G40})$$

where we used the previously defined quantities $g_{\text{eff}}^2 = \alpha r_2$ and $\text{PR}^D = r_2^2/r_4$. Eq. G40 can be solved for Ψ_{\star}^{ϕ} , yielding

$$\Psi_{\star}^{\phi} = \frac{1 + \frac{1}{\alpha \text{PR}^D} |g_{\text{eff}}^2 S_{12}^{\phi}|^2}{|1 - g_{\text{eff}}^2 S_{12}^{\phi}|^2} C_{12}^{\phi}. \quad (\text{G41})$$

This result is identical to Eq. 76 derived using the path-integral approach, demonstrating the consistency between the two methods.

Appendix H: Single-unit heterogeneity calculations

The full set of order parameters is

$$C^{\Phi}(t_1, t_2) = \frac{1}{N} \sum_i \Phi_{\boldsymbol{\theta}_i}(t_1) \Phi_{\boldsymbol{\theta}_i}(t_2), \quad \text{conjugate: } \hat{Q}(t_1, t_2); \quad (\text{H1})$$

$$Q(t_1, t_2) = \frac{1}{M} \sum_a z_a(t_1) z_a(t_2), \quad \text{conjugate: } \hat{C}^{\Phi}(t_1, t_2). \quad (\text{H2})$$

The action and single-site path integrals for this system are

$$\mathcal{S}[C^{\Phi}, \hat{C}^{\Phi}, Q, \hat{Q}] = -\frac{1}{2} C^{\Phi} \hat{Q} - \frac{1}{2} Q \hat{C}^{\Phi} - \left\langle \log W_{\boldsymbol{\theta}}[Q, \hat{Q}; \mathcal{J}] \right\rangle_{\boldsymbol{\theta}} - \alpha \left\langle \log W_D^z[C^{\Phi}, \hat{C}^{\Phi}] \right\rangle_D, \quad (\text{H3})$$

$$W_{\boldsymbol{\theta}}^x[Q, \hat{Q}; \mathcal{J}] = \int \mathcal{D}x \int \mathcal{D}\hat{x} \exp \left(i\hat{x}T[x] - \frac{1}{2} \Phi_{\boldsymbol{\theta}} \hat{Q} \Phi_{\boldsymbol{\theta}} - \frac{1}{2} \hat{x} Q \hat{x} - \frac{1}{2} \phi \mathcal{J} \phi \right), \quad (\text{H4})$$

$$W_D^z[C^{\Phi}, \hat{C}^{\Phi}] = \int \mathcal{D}z \int \mathcal{D}\hat{z} \exp \left(i\hat{z}z - \frac{1}{2} z \hat{C}^{\Phi} z - \frac{1}{2} D^2 \hat{z} C^{\Phi} \hat{z} \right). \quad (\text{H5})$$

The saddle-point calculation proceeds similarly to the non-heterogeneous case of the random-mode model. We obtain

$$\hat{C}_{\star}^{\Phi}(t_1, t_2) = \hat{Q}_{\star}(t_1, t_2) = 0, \quad (\text{H6})$$

$$C_{\star}^{\Phi}(t_1, t_2) = \langle \langle \Phi_{\boldsymbol{\theta}}(t) \Phi_{\boldsymbol{\theta}}(t') \rangle_{\star} \rangle_{\boldsymbol{\theta}}, \quad (\text{H7})$$

$$Q_{\star}(t_1, t_2) = \alpha \langle \langle z(t_1) z(t_2) \rangle_{\star D} \rangle_D, \quad (\text{H8})$$

where $\langle \dots \rangle_{\star}$ and $\langle \dots \rangle_{\star D}$ are averages with respect to $W_{\boldsymbol{\theta}}^x[Q_{\star}, 0; 0]$ and $W_D^z[C_{\star}^{\Phi}, 0]$, respectively (note that $W_{\boldsymbol{\theta}}^x[Q_{\star}, 0; 0]$ does not depend on $\boldsymbol{\theta}$). Using $\langle z(t_1) z(t_2) \rangle_{\star D} = D^2 C_{\star}^{\Phi}(t_1, t_2)$ and, consequently, $Q_{\star}(t_1, t_2) = \alpha r_2 C_{\star}^{\Phi}(t_1, t_2)$, the self-consistent problem that determines $C_{\star}^{\Phi}(t_1, t_2)$ is given by Eq. 89 and the preceding description in Sec. VI.

The frequency-dependent Hessian at the saddle point is

$$\mathbf{H} = \left(\begin{array}{cc|cc} 0 & \alpha r_2 & 0 & -1 \\ \alpha r_2 & -\alpha r_4 C_{12}^\Phi & -1 & 0 \\ \hline 0 & -1 & 0 & (\mathfrak{s}_{12}^\Phi)^* \\ -1 & 0 & \mathfrak{s}_{12}^\Phi & -\mathfrak{c}_{12}^\Phi \end{array} \right), \quad (\text{H9})$$

where the new \mathfrak{F} -raktur variables are defined in Eq. 90. We invert the Hessian using Eq. F1 and identify the upper-left element as Eq. 91. Combining the inverted Hessian with the relevant quantities for computing fluctuations of normalized variables,

$$\frac{\delta^2 S}{\delta \mathcal{J}^2} = -C_{12}^\phi, \quad \frac{\delta^2 S}{\delta \mathbf{C} \delta \mathcal{J}} = \begin{pmatrix} 0 \\ 0 \\ (S_{12}^\phi)^* \\ -\mathfrak{c}_{12}^{\Phi\phi} \end{pmatrix}, \quad (\text{H10})$$

where

$$\mathfrak{c}_{12}^{\Phi\phi} = \langle \langle \Phi_{\theta\phi} \rangle_\star(\omega_1) \langle \Phi_{\theta\phi} \rangle_\star(\omega_2) \rangle_\theta, \quad (\text{H11})$$

$$S_{12}^\phi = \left\langle \frac{\delta\phi}{\delta I} \right\rangle_\star(\omega_1) \left\langle \frac{\delta\phi}{\delta I} \right\rangle_\star(\omega_2), \quad (\text{H12})$$

we obtain Eq. 92.

Appendix I: Structured mode overlaps calculations

To generate matrices \mathbf{L} and \mathbf{R} with the correlation structure of Eq. 106 and Eq. 107, we express them in terms of independent Gaussian random matrices \mathbf{X}^1 , \mathbf{X}^2 , and \mathbf{Y} , each with variance $1/N$:

$$L_{ia} = \sqrt{1 - |\rho_a|} X_{ia}^1 + \sqrt{|\rho_a|} Y_{ia}, \quad (\text{I1})$$

$$R_{ia} = \sqrt{1 - |\rho_a|} X_{ia}^2 + \text{sgn}(\rho_a) \sqrt{|\rho_a|} Y_{ia}. \quad (\text{I2})$$

We begin with the path integral containing latent variables, insert this parameterization of \mathbf{L} and \mathbf{R} , then and integrate out \mathbf{X}_1 , \mathbf{X}_2 , and \mathbf{Y} . To factorize the action over indices spanning extensive dimensions, we introduce

$$C^\phi(t_1, t_2) = \frac{1}{N} \sum_i \phi_i(t_1) \phi_i(t_2), \quad \text{conjugate: } \hat{Q}(t_1, t_2); \quad (\text{I3})$$

$$S^\phi(t_1, t_2) = \frac{1}{N} \sum_i \frac{\delta\phi_i(t_1)}{\delta I_i(t_2)}, \quad \text{conjugate: } \hat{R}(t_1, t_2); \quad (\text{I4})$$

$$Q(t_1, t_2) = \frac{1}{M} \sum_a z_a(t_1) z_a(t_2), \quad \text{conjugate: } \hat{C}^\phi(t_1, t_2); \quad (\text{I5})$$

$$R(t_1, t_2) = \frac{1}{M} \sum_a D_a \rho_a \frac{\delta z_a(t_1)}{\delta I_a(t_2)}, \quad \text{conjugate: } \hat{S}^\phi(t_1, t_2). \quad (\text{I6})$$

The resulting path integral, action, and single-site path integrals are given by:

$$Z = \int \mathcal{D}C^\phi \int \mathcal{D}\hat{C}^\phi \int \mathcal{D}S^\phi \int \mathcal{D}\hat{S}^\phi \int \mathcal{D}Q \int \mathcal{D}\hat{Q} \int \mathcal{D}R \int \mathcal{D}\hat{R} \exp\left(-NS[C^\phi, \hat{C}^\phi, S^\phi, \hat{S}^\phi, Q, \hat{Q}, R, \hat{R}]\right), \quad (\text{I7})$$

$$\mathcal{S}[C^\phi, \hat{C}^\phi, S^\phi, \hat{S}^\phi, Q, \hat{Q}, R, \hat{R}] = -\frac{1}{2}C^\phi\hat{Q} - \frac{1}{2}Q\hat{C}^\phi + \frac{1}{2}S^\phi\hat{R} + \frac{1}{2}R\hat{S}^\phi \quad (\text{I8})$$

$$- \log W^x[Q, \hat{Q}, R, \hat{R}] - \alpha \left\langle \log W_{D,\rho}^z[C^\phi, \hat{C}^\phi, S^\phi, \hat{S}^\phi] \right\rangle_{D,\rho}, \quad (\text{I9})$$

$$W^x[Q, \hat{Q}, R, \hat{R}] = \int \mathcal{D}x \int \mathcal{D}\hat{x} \exp\left(i\hat{x}T[x] - \frac{1}{2}\hat{x}Q\hat{x} - \frac{1}{2}\phi\hat{Q}\phi - \frac{i}{2}\hat{x}R\phi - \frac{i}{2}\phi\hat{R}\hat{x}\right), \quad (\text{I10})$$

$$W_{D,\rho}^z[C^\phi, \hat{C}^\phi, S^\phi, \hat{S}^\phi] = \int \mathcal{D}z \int \mathcal{D}\hat{z} \exp\left(i\hat{z}z - \frac{1}{2}D^2\hat{z}C^\phi\hat{z} - \frac{1}{2}z\hat{C}^\phi z - \frac{i}{2}D\rho\hat{z}S^\phi z - \frac{i}{2}D\rho z\hat{S}^\phi\hat{z}\right). \quad (\text{I11})$$

We first calculate the saddle point conditions by taking the derivatives of the action:

$$\frac{\delta\mathcal{S}}{\delta C^\phi(t_1, t_2)} = -\hat{Q}(t_1, t_2) + \alpha \left\langle D^2 \langle \hat{z}(t_1)\hat{z}(t_2) \rangle_{W_{D,\rho}^z} \right\rangle_{D,\rho}, \quad (\text{I12})$$

$$\frac{\delta\mathcal{S}}{\delta \hat{C}^\phi(t_1, t_2)} = -Q(t_1, t_2) + \alpha \left\langle \langle z(t_1)z(t_2) \rangle_{W_{D,\rho}^z} \right\rangle_{D,\rho}, \quad (\text{I13})$$

$$\frac{\delta\mathcal{S}}{\delta S^\phi(t_1, t_2)} = \hat{R}(t_1, t_2) + i\alpha \left\langle D\rho \langle \hat{z}(t_1)z(t_2) \rangle_{W_{D,\rho}^z} \right\rangle_{D,\rho}, \quad (\text{I14})$$

$$\frac{\delta\mathcal{S}}{\delta \hat{S}^\phi(t_1, t_2)} = R(t_1, t_2) + i\alpha \left\langle D\rho \langle z(t_1)\hat{z}(t_2) \rangle_{W_{D,\rho}^z} \right\rangle_{D,\rho}, \quad (\text{I15})$$

$$\frac{\delta\mathcal{S}}{\delta Q(t_1, t_2)} = -\hat{C}^\phi(t_1, t_2) + \langle \hat{x}(t_1)\hat{x}(t_2) \rangle_{W^x}, \quad (\text{I16})$$

$$\frac{\delta\mathcal{S}}{\delta \hat{Q}(t_1, t_2)} = -C^\phi(t_1, t_2) + \langle \phi(t_1)\phi(t_2) \rangle_{W^x}, \quad (\text{I17})$$

$$\frac{\delta\mathcal{S}}{\delta R(t_1, t_2)} = \hat{S}^\phi(t_1, t_2) + i \langle \hat{x}(t_1)\phi(t_2) \rangle_{W^x}, \quad (\text{I18})$$

$$\frac{\delta\mathcal{S}}{\delta \hat{R}(t_1, t_2)} = S^\phi(t_1, t_2) + i \langle \phi(t_1)\hat{x}(t_2) \rangle_{W^x}. \quad (\text{I19})$$

The saddle-point conditions yield:

$$\hat{C}^\phi(t_1, t_2) = \hat{Q}_*(t_1, t_2) = 0, \quad (\text{I20})$$

$$C^\phi(t_1, t_2) = \langle \phi(t_1)\phi(t_2) \rangle_*, \quad (\text{I21})$$

$$S^\phi_*(t_1, t_2) = \hat{S}^\phi_*(t_1, t_2) = \left\langle \frac{\delta\phi(t_1)}{\delta I(t_2)} \right\rangle_*, \quad (\text{I22})$$

$$Q_*(t_1, t_2) = \alpha \left\langle \langle z(t_1)z(t_2) \rangle_{*D,\rho} \right\rangle_{D,\rho}, \quad (\text{I23})$$

$$R_*(t_1, t_2) = \hat{R}_*(t_1, t_2) = \alpha \left\langle D\rho \left\langle \frac{\delta z(t_1)}{\delta I(t_2)} \right\rangle_{*D,\rho} \right\rangle_{D,\rho}, \quad (\text{I24})$$

where $\langle \dots \rangle_{*D,\rho}$ and $\langle \dots \rangle_*$ are averages within the dynamic processes described by $W_{D,\rho}^z[C^\phi_*, 0, S^\phi_*, \hat{S}^\phi_*]$ and $W^x[Q_*, 0, R_*, \hat{R}_*]$, respectively. The yields neuronal and latent-variable single-site processes described by

$$T[x](t) = \eta^x(t) + [R_* * \phi](t) \quad (\text{I25})$$

$$z(t) = \eta^z(t) + D\rho[S^\phi_* * z](t), \quad (\text{I26})$$

where the Gaussian fields have statistics

$$\eta^x \sim \mathcal{GP}(0, Q_\star), \quad (\text{I27})$$

$$\eta^z \sim \mathcal{GP}(0, D^2 C_\star^\phi). \quad (\text{I28})$$

This gives rise to the single-site problem described in [Sec. VII](#).

The frequency-dependent Hessian at the saddle point is

$$\mathbf{H} = \left(\begin{array}{cccc|cccc} 0 & u^* & 0 & 0 & 0 & -1 & 0 & 0 \\ u & -vC_1^\phi C_2^\phi & x_{12}C_2 & x_{21}C_1^\phi & -1 & 0 & 0 & 0 \\ 0 & x_{12}^* C_2^\phi & 0 & -w & 0 & 0 & 0 & 1 \\ 0 & x_{21}^* C_1^\phi & -w^* & 0 & 0 & 0 & 1 & 0 \\ \hline 0 & -1 & 0 & 0 & 0 & (S_1^\phi S_2^\phi)^* & 0 & 0 \\ -1 & 0 & 0 & 0 & S_1^\phi S_2^\phi & -C_1^\phi C_2^\phi & S_1^\phi C_2^\phi & S_2^\phi C_1^\phi \\ 0 & 0 & 0 & 1 & 0 & (S_1^\phi)^* C_2^\phi & 0 & -(S_1^\phi)^* S_2^\phi \\ 0 & 0 & 1 & 0 & 0 & (S_2^\phi)^* C_1^\phi & -S_1^\phi (S_2^\phi)^* & 0 \end{array} \right) \quad (\text{I29})$$

where

$$u = \alpha \langle D^2 \sigma_1 \sigma_2 \rangle_{D, \rho}, \quad (\text{I30})$$

$$v = \alpha \langle D^4 |\sigma_1|^2 |\sigma_2|^2 \rangle_{D, \rho}, \quad (\text{I31})$$

$$w = \alpha \langle D^2 \rho^2 \sigma_1^* \sigma_2 \rangle_{D, \rho}, \quad (\text{I32})$$

$$x_{12} = \alpha \langle D^3 \rho \sigma_1 |\sigma_2|^2 \rangle_{D, \rho}, \quad (\text{I33})$$

$$\sigma_k = \frac{1}{1 - D\rho S_k^\phi} \text{ for } k = 1, 2. \quad (\text{I34})$$

Isolating the upper-left element of the inverse of this matrix yields [Eq. 114](#).

Appendix J: Numerical details

1. Numerics for theory

To validate the theory, we used networks with dynamics defined by $T[x](t) = (1 + \partial_t)x(t)$ ([Eq. 2](#)) and with nonlinearity $\phi(x) = \text{erf}(\sqrt{\pi}x/2)$. For all connectivity models, except those with structured \mathbf{L} - \mathbf{R} overlaps ([VII](#)), the single-site two-point functions $C_\star^\phi(\tau)$ and $S_\star^\phi(\tau)$ depend only on g_{eff} and can be numerically calculated as in i.i.d. networks (see, e.g., [[10](#), [77](#)]). In summary:

1. Since $\eta(t)$ is Gaussian, so is $x(t)$ for this linear form of $T[\cdot]$, allowing us to write $C_\star^\phi(\tau)$ in terms of Gaussian integrals over $x(t)$ and $x(t + \tau)$, which have marginal variance $C_\star^\phi(0)$ and covariance $C_\star^\phi(\tau)$. Due to our choice of $\phi(x)$, this expression simplifies to

$$C_\star^\phi(\tau) = \frac{2}{\pi} \tan^{-1} \left[\frac{C_\star^x(\tau)}{\sqrt{(C_\star^x(0) + \frac{2}{\pi})^2 - C_\star^x(\tau)^2}} \right]. \quad (\text{J1})$$

2. Squaring the single-site picture gives a second-order ODE $\partial_\tau^2 C_\star^x(\tau) = C_\star^x(\tau) - g_{\text{eff}}^2 C_\star^\phi(\tau)$. Since the rhs depends only on $C_\star^x(\tau)$ and $C_\star^x(0)$, we can consider it to be the negative derivative $-\partial V / \partial C_\star^x(\tau)$ of a potential $V(C_\star^x(\tau), C_\star^x(0))$ with an explicit dependence on the initial condition $C_\star^x(0)$.
3. The rhs is integrated w.r.t. $C_\star^x(\tau)$ to provide an expression for $V(C_\star^x(\tau), C_\star^x(0))$, which due to our choice of $\phi(x)$

simplifies to

$$V(C_\star^x(\tau), C_\star^x(0)) = -\frac{1}{2}C_\star^x(\tau)^2 + g_{\text{eff}}^2 \left[\frac{2}{\pi} \sqrt{\left(C_\star^x(0) + \frac{2}{\pi} \right)^2 - C_\star^x(\tau)^2} + C_\star^x(\tau) C_\star^\phi(\tau) \right]. \quad (\text{J2})$$

4. Restricting to solutions with $C_\star^x(\tau) \rightarrow 0$ as $\tau \rightarrow \infty$ and $\partial_\tau C_\star^x(\tau)|_{\tau=0} = 0$, enforcing conservation of energy gives $V(C_\star^x(0), C_\star^x(0)) = V(0, C_\star^x(0))$, which can be solved for $C_\star^x(0)$ by numerical root finding.
5. Finally, Euler integration of the $[C_\star^x(\tau), \partial_\tau C_\star^x(\tau)]$ dynamics with these initial conditions gives its full time course, along with $C_\star^\phi(\tau)$ via [Eq. J1](#).

We integrated the Newtonian ODE from $\tau = 0$ to $\tau_{\text{max}} = 200$ with step size $d\tau = 0.025$. When then use an FFT to obtain the frequency-space representation. The frequency-space representation of the response function $S_\star^\phi(\omega)$ was computed directly as

$$S_\star^\phi(\omega) = \frac{\langle \phi' \rangle_\star}{1 + i\omega}, \quad (\text{J3})$$

with $\langle \phi' \rangle_\star = 1/\sqrt{1 + (\pi/2)C_\star^x(0)}$. Various expressions for $\Psi_\star^a(\omega_1, \omega_2)$ were then computed in frequency space before transforming back to the time domain by a 2D inverse FFT.

For structured **L-R** overlaps, the $\mathcal{O}(1)$ self-coupling in the single-site process makes $x(t)$ non-Gaussian, preventing the use of Gaussian integrals in the DMFT solution. We there obtain the solution via standard numerical methods, enforcing self-consistency among the $\eta^x(t)$ autocovariance function, $Q_\star(\tau)$; the self-coupling kernel, $R_\star(\tau)$; the response function, $S_\star^\phi(\tau)$; and the $\phi(t)$ autocovariance function, $C_\star^\phi(\tau)$. In summary:

1. Seed values for kernels are set as $C_0^\phi(\tau) = \exp[-(\tau/15)^2] + 10^{-4}\delta(\tau)$ and $S_0^\phi(\tau) = 0$.
2. $Q_0(\tau)$ and $R_0(\tau)$ are computed in Fourier space using the current values of $C_0^\phi(\tau)$ and $S_0^\phi(\tau)$ via [Eq. 112](#), with the average taken over (D, ρ) .
3. A set of $N_{\text{sample}} = 10^4$ instances of η^x are sampled according to the Gaussian process kernel $Q_0(\tau)$ by standard spectral methods.
4. Each of N_{sample} single-site processes $x_s(t)$ is Euler integrated according to [Eq. 110](#) with the input $\eta_s^x(t)$ and self-feedback by the convolution between $R_0(\tau)$ and $\phi(x_s(t))$.
5. These time series $\phi(x_s(t))$ and $\eta_s^x(t)$ are used to compute empirical values $(C_1^\phi(\tau), S_1^\phi(\tau))$ for the autocovariance and response. The latter is computed by the Furutsu-Novikov theorem: $S^\phi(\omega) = C^{\phi\eta}(\omega)/C^\eta(\omega)$. The numerator is estimated using these time series, while $C^\eta(\omega)$ is simply $Q_0(\omega)$.
6. After $N_{\text{iter}} = 300$ repetitions of steps (1)-(5) with smoothed updates

$$C_m^\phi(\tau) \leftarrow 0.2C_{m-1}^\phi(\tau) + 0.8C_m^\phi(\tau) \quad (\text{J4})$$

$$S_m^\phi(\tau) \leftarrow 0.2S_{m-1}^\phi(\tau) + 0.8S_m^\phi(\tau) \quad (\text{J5})$$

as new seed values for the upcoming m th iteration, the final numerical estimates for $C_\star^\phi(\tau)$ and $S_\star^\phi(\tau)$ are computed as the averages over the last 50 iterations.

We used a temporal discretization $\tau_{\text{max}} = 120$, $d\tau = 0.04$. With these quantities, the various components of [Eq. 114](#) and the expression for Ψ_\star^ϕ are straightforward to compute. We took $\langle \cdot \rangle_{D, \rho}$ averages in this case by averaging over every other discrete value of D_a and ρ_a .

2. Simulation details

Each network was integrated via Runge-Kutta (RK4) with $dt = 0.05$. The empirical lagged covariance matrix was computed by averaging over N_{loop} individual covariance estimates, each of which is based on $T = 2000$ discrete, evenly

spaced time samples $t_k^{i_{\text{loop}}}$, with $t_k^{i_{\text{loop}}} - t_{k-1}^{i_{\text{loop}}} = 1$:

$$\widehat{C_{ij}^{\phi}(\tau)} = \left\langle \frac{1}{T-1} \sum_{k=1}^T \phi_i(t_k^{i_{\text{loop}}}) \phi_j(t_k^{i_{\text{loop}}} - \tau) \right\rangle_{i_{\text{loop}}=1}^{N_{\text{loop}}}. \quad (\text{J6})$$

The value of N_{loop} varied but was generally ≥ 50 and always chosen to ensure saturated dimension values, i.e. $TN_{\text{loop}} \gg N$. Specific quantities of interest, such as PR^{ϕ} or $\Psi^{\phi}(\tau, 0)$, were computed using this estimate.

-
- [1] O. Barak, D. Sussillo, R. Romo, M. Tsodyks, and L. Abbott, From fixed points to chaos: three models of delayed discrimination, *Progress in neurobiology* **103**, 214 (2013).
- [2] V. Mante, D. Sussillo, K. V. Shenoy, and W. T. Newsome, Context-dependent computation by recurrent dynamics in prefrontal cortex, *nature* **503**, 78 (2013).
- [3] D. Sussillo, M. M. Churchland, M. T. Kaufman, and K. V. Shenoy, A neural network that finds a naturalistic solution for the production of muscle activity, *Nature neuroscience* **18**, 1025 (2015).
- [4] S. Hochreiter and J. Schmidhuber, Long short-term memory, *Neural computation* **9**, 1735 (1997).
- [5] I. Sutskever, O. Vinyals, and Q. V. Le, Sequence to sequence learning with neural networks, *Advances in neural information processing systems* **27** (2014).
- [6] K. Cho, B. Van Merriënboer, C. Gulcehre, D. Bahdanau, F. Bougares, H. Schwenk, and Y. Bengio, Learning phrase representations using rnn encoder-decoder for statistical machine translation, *arXiv preprint arXiv:1406.1078* (2014).
- [7] K. Krishnamurthy, T. Can, and D. J. Schwab, Theory of gating in recurrent neural networks, *Physical Review X* **12**, 011011 (2022).
- [8] K. Rajan, L. Abbott, and H. Sompolinsky, Stimulus-dependent suppression of chaos in recurrent neural networks, *Physical Review E* **82**, 011903 (2010).
- [9] R. Engelken, F. Wolf, and L. F. Abbott, Lyapunov spectra of chaotic recurrent neural networks, *Physical Review Research* **5**, 043044 (2023).
- [10] H. Sompolinsky, A. Crisanti, and H.-J. Sommers, Chaos in random neural networks, *Physical Review Letters* **61**, 259 (1988).
- [11] D. Sussillo and L. Abbott, Generating coherent patterns of activity from chaotic neural networks, *Neuron* **63**, 544 (2009).
- [12] R. Laje and D. V. Buonomano, Robust timing and motor patterns by taming chaos in recurrent neural networks, *Nature neuroscience* **16**, 925 (2013).
- [13] J. Aljadeff, M. Stern, and T. Sharpee, Transition to chaos in random networks with cell-type-specific connectivity, *Physical Review Letters* **114**, 088101 (2015).
- [14] S. Song, P. J. Sjöström, M. Reigl, S. Nelson, and D. B. Chklovskii, Highly nonrandom features of synaptic connectivity in local cortical circuits, *PLoS biology* **3**, e68 (2005).
- [15] V. Thibeault, A. Allard, and P. Desrosiers, The low-rank hypothesis of complex systems, *Nature Physics* **20**, 294 (2024).
- [16] I. Akjouj, M. Barbier, M. Clenet, W. Hachem, M. Maïda, F. Massol, J. Najim, and V. C. Tran, Complex systems in ecology: a guided tour with large lotka-volterra models and random matrices, *Proceedings of the Royal Society A* **480**, 20230284 (2024).
- [17] Z. Wang, W. Mai, Y. Chai, K. Qi, H. Ren, C. Shen, S. Zhang, G. Tan, Y. Hu, and Q. Wen, The geometry and dimensionality of brain-wide activity, *bioRxiv* (2024).
- [18] L. Pezon, V. Schmutz, and W. Gerstner, Linking neural manifolds to circuit structure in recurrent networks, *bioRxiv*, 2024 (2024).
- [19] F. Schuessler, F. Mastrogiuseppe, A. Dubreuil, S. Ostojic, and O. Barak, The interplay between randomness and structure during learning in rnns, *Advances in Neural Information Processing Systems* **33**, 13352 (2020).
- [20] C. H. Martin and M. W. Mahoney, Implicit self-regularization in deep neural networks: evidence from random matrix theory and implications for learning., *J. Mach. Learn. Res.* **22**, 1 (2021).
- [21] L. K. Scheffer, C. S. Xu, M. Januszewski, Z. Lu, S.-y. Takemura, K. J. Hayworth, G. B. Huang, K. Shinomiya, J. Maitlin-Shepard, S. Berg, *et al.*, A connectome and analysis of the adult drosophila central brain, *elife* **9**, e57443 (2020).
- [22] N. Eckstein, A. S. Bates, A. Champion, M. Du, Y. Yin, P. Schlegel, A. K.-Y. Lu, T. Rymer, S. Finley-May, T. Patterson, *et al.*, Neurotransmitter classification from electron microscopy images at synaptic sites in drosophila melanogaster, *Cell* **187**, 2574 (2024).
- [23] P. Gao and S. Ganguli, On simplicity and complexity in the brave new world of large-scale neuroscience, *Current Opinion in Neurobiology* **32**, 148 (2015).
- [24] S. Chung and L. Abbott, Neural population geometry: An approach for understanding biological and artificial neural networks, *Current Opinion in Neurobiology* **70**, 137 (2021).
- [25] D. G. Clark, L. Abbott, and A. Litwin-Kumar, Dimension of activity in random neural networks, *Physical Review Letters* **131**, 118401 (2023).
- [26] D. Dahmen, S. Grün, M. Diesmann, and M. Helias, Second type of criticality in the brain uncovers rich multiple-neuron dynamics, *Proceedings of the National Academy of Sciences* **116**, 13051 (2019).
- [27] Y. Hu and H. Sompolinsky, The spectrum of covariance matrices of randomly connected recurrent neuronal networks with linear dynamics, *PLoS Computational Biology* **18**, 1 (2022).
- [28] Y.-L. Shi, R. Zeraati, A. Levina, and T. A. Engel, Spatial

- and temporal correlations in neural networks with structured connectivity, *Physical Review Research* **5**, 013005 (2023).
- [29] M. Layer, M. Helias, and D. Dahmen, Effect of synaptic heterogeneity on neuronal coordination, *PRX life* **2**, 013013 (2024).
- [30] F. Mastrogiuseppe and S. Ostojic, Linking connectivity, dynamics, and computations in low-rank recurrent neural networks, *Neuron* **99**, 609 (2018).
- [31] M. Beiran, A. Dubreuil, A. Valente, F. Mastrogiuseppe, and S. Ostojic, Shaping dynamics with multiple populations in low-rank recurrent networks, *Neural Computation* **33**, 1572 (2021).
- [32] A. Litwin-Kumar, K. D. Harris, R. Axel, H. Sompolinsky, and L. Abbott, Optimal degrees of synaptic connectivity, *Neuron* **93**, 1153 (2017).
- [33] S. P. Muscinelli, M. J. Wagner, and A. Litwin-Kumar, Optimal routing to cerebellum-like structures, *Nature neuroscience* **26**, 1630 (2023).
- [34] K. Rajan, L. Abbott, and H. Sompolinsky, Inferring stimulus selectivity from the spatial structure of neural network dynamics, *Advances in Neural Information Processing Systems* **23** (2010).
- [35] L. Abbott, K. Rajan, and H. Sompolinsky, Interactions between intrinsic and stimulus-evoked activity in recurrent neural networks, in *The dynamic brain: an exploration of neuronal variability and its functional significance*, edited by M. Ding and D. Glanzman (Oxford University Press, 2011) p. 65–82.
- [36] P. Gao, E. Trautmann, B. Yu, G. Santhanam, S. Ryu, K. Shenoy, and S. Ganguli, A theory of multineuronal dimensionality, dynamics and measurement, *bioRxiv* , 214262 (2017).
- [37] S. Recanatesi, G. K. Ocker, M. A. Buice, and E. Shea-Brown, Dimensionality in recurrent spiking networks: Global trends in activity and local origins in connectivity, *PLoS Computational Biology* **15**, e1006446 (2019).
- [38] S. Recanatesi, S. Bradde, V. Balasubramanian, N. A. Steinmetz, and E. Shea-Brown, A scale-dependent measure of system dimensionality, *bioRxiv* (2020).
- [39] M. Mézard, G. Parisi, and M. A. Virasoro, *Spin glass theory and beyond: An Introduction to the Replica Method and Its Applications*, Vol. 9 (World Scientific Publishing Company, 1987).
- [40] A. Crisanti and H. Sompolinsky, Path integral approach to random neural networks, *Physical Review E* **98**, 062120 (2018).
- [41] M. Helias and D. Dahmen, *Statistical field theory for neural networks*, Vol. 970 (Springer, 2020).
- [42] R. Price, A useful theorem for nonlinear devices having gaussian inputs, *IRE Transactions on Information Theory* **4**, 69 (1958).
- [43] A. Ingrosso, Optimal learning with excitatory and inhibitory synapses, *PLOS Computational Biology* **16**, e1008536 (2020).
- [44] J. Pennington, S. Schoenholz, and S. Ganguli, Resurrecting the sigmoid in deep learning through dynamical isometry: theory and practice, *Advances in neural information processing systems* **30** (2017).
- [45] J. Pennington, S. Schoenholz, and S. Ganguli, The emergence of spectral universality in deep networks, in *International Conference on Artificial Intelligence and Statistics* (PMLR, 2018) pp. 1924–1932.
- [46] F. Schuessler, A. Dubreuil, F. Mastrogiuseppe, S. Ostojic, and O. Barak, Dynamics of random recurrent networks with correlated low-rank structure, *Physical Review Research* **2**, 013111 (2020).
- [47] A. Dubreuil, A. Valente, M. Beiran, F. Mastrogiuseppe, and S. Ostojic, The role of population structure in computations through neural dynamics, *Nature neuroscience* **25**, 783 (2022).
- [48] S. Mei, A. Montanari, and P.-M. Nguyen, A mean field view of the landscape of two-layer neural networks, *Proceedings of the National Academy of Sciences* **115**, E7665 (2018).
- [49] L. Chizat, E. Oyallon, and F. Bach, On lazy training in differentiable programming, in *Advances in Neural Information Processing Systems*, Vol. 32, edited by H. Wallach, H. Larochelle, A. Beygelzimer, F. d'Alché-Buc, E. Fox, and R. Garnett (Curran Associates, Inc., 2019).
- [50] B. Woodworth, S. Gunasekar, J. D. Lee, E. Moroshko, P. Savarese, I. Golan, D. Soudry, and N. Srebro, Kernel and rich regimes in overparametrized models, in *Proceedings of Thirty Third Conference on Learning Theory*, Proceedings of Machine Learning Research, Vol. 125, edited by J. Abernethy and S. Agarwal (PMLR, 2020) pp. 3635–3673.
- [51] A. van Meegen and H. Sompolinsky, Coding schemes in neural networks learning classification tasks, *arXiv preprint arXiv:2406.16689* (2024).
- [52] Q. Li and H. Sompolinsky, Statistical mechanics of deep linear neural networks: The backpropagating kernel renormalization, *Physical Review X* **11**, 031059 (2021).
- [53] D. A. Roberts, S. Yaida, and B. Hanin, *The principles of deep learning theory*, Vol. 46 (Cambridge University Press Cambridge, MA, USA, 2022).
- [54] J. Zinn-Justin, *Quantum field theory and critical phenomena*, Vol. 171 (Oxford university press, 2021).
- [55] M. Moshe and J. Zinn-Justin, Quantum field theory in the large n limit: A review, *Physics Reports* **385**, 69 (2003).
- [56] G. K. Ocker, Republished: Dynamics of stochastic integrate-and-fire networks, *Physical Review X* **13**, 041047 (2023).
- [57] J. A. Hertz, Y. Roudi, and P. Sollich, Path integral methods for the dynamics of stochastic and disordered systems, *Journal of Physics A: Mathematical and Theoretical* **50**, 033001 (2016).
- [58] W. Zou and H. Huang, Introduction to dynamical mean-field theory of randomly connected neural networks with bidirectionally correlated couplings, *SciPost Physics Lecture Notes* , 079 (2024).
- [59] A. van Meegen, T. Kühn, and M. Helias, Large-deviation approach to random recurrent neuronal networks: Parameter inference and fluctuation-induced transitions, *Physical Review Letters* **127**, 158302 (2021).
- [60] Note that the variance of $\eta^z(t)$ is scaled by D^2 ; equivalently, we could factor out D^2 from the variance and include D as a multiplicative factor in the latent-variable single-site dynamics (Eq. 71).
- [61] M. Mézard, The space of interactions in neural networks: Gardner's computation with the cavity method, *Journal of Physics A: Mathematical and General* **22**, 2181 (1989).
- [62] M. Mézard, Mean-field message-passing equations in the hopfield model and its generalizations, *Physical Review E* **95**, 022117 (2017).
- [63] T. Hromádka, M. R. DeWeese, and A. M. Zador, Sparse representation of sounds in the unanesthetized auditory cortex, *PLoS biology* **6**, e16 (2008).

- [64] M. Stern, H. Sompolinsky, and L. F. Abbott, Dynamics of random neural networks with bistable units, *Physical Review E* **90**, 062710 (2014).
- [65] A. Litwin-Kumar and B. Doiron, Slow dynamics and high variability in balanced cortical networks with clustered connections, *Nature Neuroscience* **15**, 1498 (2012).
- [66] G. R. Yang, M. R. Joglekar, H. F. Song, W. T. Newsome, and X.-J. Wang, Task representations in neural networks trained to perform many cognitive tasks, *Nature neuroscience* **22**, 297 (2019).
- [67] L. N. Driscoll, K. Shenoy, and D. Sussillo, Flexible multitask computation in recurrent networks utilizes shared dynamical motifs, *Nature Neuroscience* , 1 (2024).
- [68] R. Milo, S. Shen-Orr, S. Itzkovitz, N. Kashtan, D. Chklovskii, and U. Alon, Network motifs: simple building blocks of complex networks, *Science* **298**, 824 (2002).
- [69] Y. Hu, J. Trousdale, K. Josić, and E. Shea-Brown, Motif statistics and spike correlations in neuronal networks, *Journal of Statistical Mechanics: Theory and Experiment* **2013**, P03012 (2013).
- [70] P. V. Aceituno, T. Rogers, and H. Schomerus, Universal hypotrochoidic law for random matrices with cyclic correlations, *Physical Review E* **100**, 010302 (2019).
- [71] L. F. Abbott, D. D. Bock, E. M. Callaway, W. Denk, C. Dulac, A. L. Fairhall, I. Fiete, K. M. Harris, M. Helmsstaedter, V. Jain, *et al.*, The mind of a mouse, *Cell* **182**, 1372 (2020).
- [72] L. Tiberi, D. Dahmen, and M. Helias, Hidden connectivity structures control collective network dynamics, *arXiv preprint arXiv:2303.02476* (2023).
- [73] V. Schmutz, J. Brea, and W. Gerstner, Emergent rate-based dynamics in duplicate-free populations of spiking neurons, *arXiv preprint arXiv:2303.05174* (2023).
- [74] Z. Lin and H. Huang, Spiking mode-based neural networks, *Physical Review E* **110**, 024306 (2024).
- [75] C. Teeter, R. Iyer, V. Menon, N. Gouwens, D. Feng, J. Berg, A. Szafer, N. Cain, H. Zeng, M. Hawrylycz, *et al.*, Generalized leaky integrate-and-fire models classify multiple neuron types, *Nature communications* **9**, 709 (2018).
- [76] E. Marder and J.-M. Goaillard, Variability, compensation and homeostasis in neuron and network function, *Nature Reviews Neuroscience* **7**, 563 (2006).
- [77] F. Mastrogiuseppe, *From dynamics to computations in recurrent neural networks*, Ph.D. thesis, Université Paris sciences et lettres (2017).